High Power Laser Science and Engineering, (2019), Vol. 7, e50, 21 pages.

doi:10.1017/hpl.2019.35

High-repetition-rate ($\geqslant$ kHz) targets and optics from liquid microjets for high-intensity laser–plasma interactions

K. M. George[1], J. T. Morrison[1], S. Feister[2,3], G. K. Ngirmang[4,5], J. R. Smith[6], A. J. Klim[6], J. Snyder[7], D. Austin[6], W. Erbsen[1], K. D. Frische[1], J. Nees[8], C. Orban[6], E. A. Chowdhury[6,9], and W. M. Roquemore[5]

[1]*Innovative Scientific Solutions, Inc., Dayton, Ohio 45459, USA*

[2]*Department of Physics and Astronomy, University of California, Los Angeles, California 90095, USA*

[3]*Computer Science Program and Applied Physics Program, California State University Channel Islands, Camarillo, California 93012, USA*

[4]*National Academies of Science, Engineering, and Medicine, Washington, DC 20001, USA*

[5]*Air Force Research Laboratory, WPAFB, Ohio 45433, USA*

[6]*Department of Physics, Ohio State University, Columbus, Ohio 43210, USA*

[7]*Department of Mathematical and Physical Sciences, Miami University, Hamilton, Ohio 45011, USA*

[8]*Center for Ultrafast Optical Sciences, University of Michigan, Ann Arbor, Michigan 48109, USA*

[9]*Intense Energy Solutions, LLC., Plain City, Ohio 43064, USA*

(Received 21 February 2019; revised 22 May 2019; accepted 20 June 2019)

Abstract

High-intensity laser–plasma interactions produce a wide array of energetic particles and beams with promising applications. Unfortunately, the high repetition rate and high average power requirements for many applications are not satisfied by the lasers, optics, targets, and diagnostics currently employed. Here, we aim to address the need for high-repetition-rate targets and optics through the use of liquids. A novel nozzle assembly is used to generate high-velocity, laminar-flowing liquid microjets which are compatible with a low-vacuum environment, generate little to no debris, and exhibit precise positional and dimensional tolerances. Jets, droplets, submicron-thick sheets, and other exotic configurations are characterized with pump–probe shadowgraphy to evaluate their use as targets. To demonstrate a high-repetition-rate, consumable, liquid optical element, we present a plasma mirror created by a submicron-thick liquid sheet. This plasma mirror provides etalon-like anti-reflection properties in the low field of 0.1% and high reflectivity as a plasma, 69%, at a repetition rate of 1 kHz. Practical considerations of fluid compatibility, in-vacuum operation, and estimates of maximum repetition rate are addressed. The targets and optics presented here demonstrate a potential technique for enabling the operation of laser–plasma interactions at high repetition rates.

Keywords: high intensity; high repetition rate; laser–plasma interaction; liquid droplet; liquid microjet; liquid sheet; plasma mirror; target

1. Introduction

Relativistically intense laser–plasma interactions are capable of generating energetic sources of radiation and particles. X-ray, gamma ray, electron, positron, proton, heavy ion, and neutron sources stemming from these interactions have all been created and characterized[1–18]. These sources are advantageous for a range of applications, due to the small source sizes[19–21] and short time durations[22] which are unmatched by conventional techniques. Additionally, a single, table-top laser system can be used to generate a wide array of energetic particles and beams[23, 24].

Facilities capable of reaching relativistic intensities have been available at laboratories around the world for decades. Using these systems, numerous radiation generation and particle acceleration mechanisms have been discovered and studied, including attosecond pulse production[25, 26], electron bunch acceleration in reflection[27–29] and transmission[30, 31], ion acceleration with target normal sheath

Correspondence to: K. M. George. Innovative Scientific Solutions, Inc., 7610 McEwen Rd., Dayton, Ohio 45459, USA. Email: kmgeorge88@gmail.com

acceleration[1, 2], transverse ion acceleration[32, 33], light-sail[3, 4], breakout afterburner[5], and radiation pressure acceleration[6–8]. Complementary to these studies is the optimization of target element[9], shape[10], thickness[11], use of microstructured surfaces[12–15], and tailoring the preplasma scale length[16–18] which serve to enhance the particle source total number, divergence, and peak energy to meet the needs of various applications.

Of particular interest to the application of these sources is use in proton cancer therapy[34, 35], neutron generation[36, 37], and nuclear activation[38]. Unfortunately, current generation laser, target, optic, and diagnostic techniques do not meet the high repetition rate or high average power needs of these applications. Most relativistically intense laser systems today operate at low repetition rates, ranging from 1 shot per hour to 1 shot per minute, and provide average powers of less than 1 W[39].

To address these deficiencies and satisfy the requirements of numerous applications, advances in laser technology are being implemented to construct new facilities which operate with high average power and at high repetition rates[40–45]. These lasers run at between 1 and 1000 Hz and provide high average power, in excess of 100 W. Development of future road maps for petawatt-class lasers operating at kHz and higher repetition rates for advanced accelerator concepts and high-energy particle sources are already underway[46]. To use these current or future high-repetition-rate systems to their full capability, target, optic, and diagnostic technology, along with new operational techniques, must be developed[47].

Target systems designed for low-repetition-rate operation typically rely on solid metal foils which are individually rastered or rotated into place and aligned to an accuracy within a few microns before irradiation. At a 1 to 10 Hz repetition rate this process is feasible, but scaling to even higher repetition rates quickly becomes untenable. The total number of targets per carrier is typically limited to a few hundred or a thousand at most, requiring downtime to reload.

Before alignment, each target must be precisely fabricated and characterized. Use at high repetition rates requires tens to hundreds of thousands of targets for sustained operation throughout the course of just one day. Current fabrication and metrology approaches are not suited to meet the over thousand-fold increase in demand for these targets.

Another important topic to consider, as repetition rates increase, is technology to improve the properties of the ultra-intense laser pulse before it arrives at the target. Plasma mirrors, a commonly employed optical element, aim to improve the temporal pulse contrast of the laser and prevent the deleterious generation of preplasma[48]. Typically comprised of a dielectric anti-reflection coating on an optical quality substrate, plasma mirrors are one-time-use optics in which the irradiated region is destroyed on each laser shot. Large-area plasma mirrors are commonly used and rastered for multiple exposures in order to limit the cost of such devices; however, use in 1 to 10 Hz systems is impractical, purely from a cost standpoint.

High-repetition-rate operation presents new operational challenges not present with low-repetition-rate systems. As laser intensities and peak powers increase, combined with high-repetition-rate operation, the potential for debris accumulation and damage to sensitive optics increases. Exceedingly expensive final focusing optics may need to become consumable, or protected by consumable pellicles, when operating in these environments. Lower-cost, lower-quality disposable focusing optics or plasma optics have been proposed as substitutes[49].

For all of these reasons there is now a consensus that much more work needs to be done to address these concerns[47]. Earlier pioneering works had the foresight to identify and undertake many of these issues[50, 51]. In doing so, an intense, kHz repetition rate, femtosecond laser was integrated with a liquid jet target for developing integrated sources of radiation and particles. Given recent emphasis on, and developments of, relativistically intense, high-repetition-rate lasers, we bring new insights and results. This work details a high-repetition-rate mode of operation for targets and optics based on liquid microjets for the application and study of laser–plasma interactions.

Here we present a novel target generation scheme based on high-velocity, laminar-flowing, liquid microjets which support estimated repetition rates up to 40 kHz. The targets include a 33 μm diameter cylindrical jet, 21 and 55 μm diameter droplets, submicron-thick sheets, and other exotic configurations, all from a simple and robust nozzle assembly. High-repetition-rate, consumable, optical elements are demonstrated with a plasma mirror generated by use of a submicron-thick liquid sheet. Operating at a 1 kHz repetition rate in the low field, the etalon-like anti-reflection properties provide a reflectivity of 0.1%. When an intense laser pulse is incident, the triggered plasma reflectivity is 69%. We detail our efforts to practically achieve continuous operation in a low-vacuum environment, addressing fluid compatibility and maximum proposed repetition rates for each target type.

The paper is organized as follows. We begin by discussing the physics involved in the formation of liquid jets – including laminar flow conditions, limitations to the free laminar flow propagation, subsequent breakup effects – and provide characteristic lengths and timescales for the jets formed in this work. The assembly used to generate these liquid microjets is then detailed in Section 3, covering the simple and robust nozzle design along with the fluid pump employed. Section 4 examines liquid targets: cylindrical jets, droplets, submicron-thick sheets, and other geometries. Here, dimensional and positional stability, critical to experimental use, is characterized with short-pulse probe beam shadowgraphy. Section 5 covers the experimental demonstration of a liquid plasma mirror. We then discuss a number of practical considerations in the design, use and implementation of this system, including vacuum operation, fluid compatibility, and estimates for the maximum repetition rate. Lastly, the

https://doi.org/10.1017/hpl.2019.35 Published online by Cambridge University Press

paper is concluded with a discussion of the implications and impact of this work in relation to advancing the capabilities of high-repetition-rate, relativistically intense laser–plasma interactions.

2. Physics of liquid jets

The liquid targets and optics described in this work are based on the physics of liquid jets which were first studied in detail by Lord Rayleigh over 100 years ago[52]. Since that time, our collective understanding of the fundamental physical interactions of liquid jets has enabled widespread use in a range of applications from jet engine propulsion[53] to X-ray spectroscopy[54]. Here, we briefly address the physics which forms the basis of the target and optic work described later in this paper.

The fundamental component of the target system is a high-velocity, laminar-flowing, liquid microjet. Formation of a continuous, laminar-flowing liquid jet requires that the Reynolds number, R_e, as defined by $R_e = \rho v d/\eta$ where ρ is the density, v the velocity, d the diameter and η the viscosity, be less than 2000[52, 55]. Flow conditions exceeding this laminar limit generate turbulent instability in the jet, leading to premature breakup during propagation[56–58].

Even within this laminar limit, jets are inherently unstable due to the Plateau–Rayleigh instability[52]. Perturbations in the flow ultimately lead to a minimization of the surface energy which drives breakup of the jet into droplets. This effect occurs over a characteristic distance, the spontaneous breakup length, $L = 12v(\sqrt{\rho d^3/\sigma} + 3\eta d/\sigma)$, where σ is the surface tension[59, 60]. When uncontrolled, the resulting jet decomposes into a droplet spray with largely varying droplet volume and velocity distribution. This effect is detrimental to the practical application of fluid jets, as a long, stable, propagation distance is required in order to permit optical and diagnostic access to the laser–target interaction region.

In some cases, droplet formation in a repeatable manner is desired. One can provide a droplet for every laser pulse by seeding the Plateau–Rayleigh instability through vibrations or pressure fluctuations to initiate droplet formation with high repeatability. When operated in this mode, droplets are formed at repeatable intervals with well-controlled volume and velocity distributions. Additionally, the flow-dependent droplet formation frequency allows for the creation of a droplet train at repetition rates greater than 100 kHz.

Following from the Plateau–Rayleigh instability, the growth rate of a perturbation to a flowing-liquid jet is maximal at the point where $kR_0 \approx 0.697$, with k being the perturbation wavenumber defined by $k = 2\pi/\lambda$ and R_0 equal to the radius of the unperturbed liquid jet. Given a flow rate of the liquid jet, r_f, the spontaneous droplet frequency, f_d, is given by $f_d = 0.35 r_f/(\pi^2 R_0^3)$. Utilizing the droplet frequency, the droplet size, D_d, is estimated to be $D_d = 3.78R_0$. Droplets smaller than D_d, called satellite droplets, may also be formed during droplet breakoff and appear, alternating with the primary droplets in the droplet train[61].

To give a scale of these values for the parameters used in this work we operate with a nominally 30 μm diameter jet with a controlled fluid velocity of 24 m · s^{-1}. For ethylene glycol and its associated surface tension and viscosity values, $R_e = 44.7$, which is well within the laminar flow regime. The spontaneous breakup length, L, is 15.8 mm. When operated in the droplet formation mode the natural droplet size is 56.7 μm with a spontaneous droplet frequency of 178 kHz.

3. Liquid microjet assembly

Fundamental to the formation of liquid microjets in this work is our effort to adhere to ease of setup and maintenance. Therefore, many of the components in the microjet assembly are commercial off-the-shelf items which are supplied in large quantity for relatively low cost. The following section details the components of the microjet assembly and construction techniques.

The fundamental components of the liquid microjet nozzle assembly are shown in Figure 1. The nozzle assembly depicted here is comprised of a Swagelok 1/16 inch straight union, nut, Vespel ferrule, and fused silica capillary.

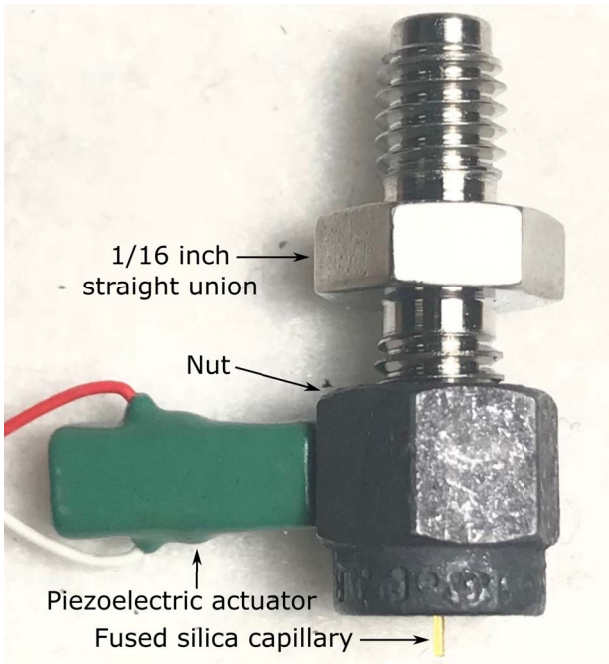

Figure 1. Liquid microjet nozzle assembly composed of a 1/16 inch Swagelok fitting, Vespel ferrule, 30 μm inner diameter glass capillary tube, and locking nut with affixed piezoelectric actuator for droplet formation.

https://doi.org/10.1017/hpl.2019.35 Published online by Cambridge University Press

A piezoelectric actuator is affixed with epoxy to the Swagelok nut for the purpose of enabling seeded droplet formation.

The Swagelok components are standard off-the-shelf items which require no modification for installation in this system. Vespel ferrules are specified to accommodate the outer diameter of the glass capillary, used as the nozzle tip, at 400 μm. The glass capillary is available for purchase by the meter with an outer diameter of 360 μm and available inner diameters ranging from 5 to over 200 μm. A Shortix fused silica capillary cutter is used to cut the capillary, which is then installed into the ferrule and Swagelok assembly by hand. Damaged or clogged nozzles can be cheaply and easily swapped out, with the only consumable items being the capillary and Vespel ferrule.

For this work we employ a glass capillary with 30 μm inner diameter. We found nozzles smaller than 25 μm require additional complications of meticulous component inspection, cleaning, and use of multiple stages of sintered steel filters along the fluid lines in order to prevent clogging. Smaller nozzle apertures also require pumps rated for pressures higher than 10,000 psi. Operating above this pressure threshold requires specialized valves, filters, fittings, and lines throughout the system. These complications and clogging failure work against the desired simple construction and robust operation of the presented system.

The high-velocity, laminar-flowing, liquid microjet from the nozzle assembly is driven by a high-pressure syringe pump, Teledyne ISCO Model 100 DX, which provides a continuous flow at up to 10,000 psi. The stable pressure control and vibration-free output of the syringe pump makes it particularly well-suited for the formation of laminar, liquid microjets. Changes in the fluid pressure supplied to the nozzle lead to variations in the laminar flow conditions essential for consistent jet formation. Further, pressure waves within the fluid lines can directly couple to vibrations at the nozzle tip which reduce alignment precision and can seed instabilities in the fluid flow, causing disintegration of the jet before the expected breakup distance.

The liquid supply for the syringe pump is maintained at atmospheric pressure and fed into the 100 mL syringe pump reservoir through a 2 μm sintered steel filter to remove particulates. From this reservoir the fluid is transported to the target chamber, at high pressure, via standard 1/16 inch Swagelok stainless steel tubing and fittings. The fluid line is connected to the nozzle assembly from Figure 1. Under the appropriate flow conditions, a high-velocity, laminar, liquid microjet is formed at the termination of the nozzle assembly capillary and used to form the targets and optics detailed in the following sections.

We note here that the operation time of the above-described configuration with a single syringe pump is limited by the 100 mL reservoir size. Thus the liquid target can operate continuously for 50 min before stopping to refill, which takes roughly 10 min. However, continuous operation with two syringe pumps is a commercially offered feature.

In the case that the fluid flow is stopped and restarted, the targets have been found to repeatedly return to their previous state. Even when irradiated at a 1 kHz repetition rate, the targets are stable after multiple refill cycles through the course of a day. Further, day after day the targets are routinely reformed with consistent and precise positional and dimensional stability, and the nozzles have been found to last for over one month before requiring replacement due to clogging or damage.

4. Liquid targets

The demands for target requirements for laser–plasma interaction (LPI) studies and applications have been discussed and detailed throughout the literature[47]. To review, targets must be thin, of the order of 10 μm or less, and allow for variable thickness capability, as thin as tens of nanometers, for optimization of certain physical mechanisms such as breakout afterburner or radiation pressure acceleration. Due to fast-focusing optics, alignment along the optical axis must be maintained within tolerances of a few microns. Lastly, the target must operate at a low ambient pressure to prevent nonlinear phase effects from impacting the beam propagation to the target[62, 63]. Additional constraints imposed for high-repetition-rate targets are debris-free operation and low cost per shot.

Previous efforts to operate with solid density targets at high repetition rates include ribbon spools[64, 65] and rotating disks[66, 67]. These targets are typically thicker than 10 μm and thus are not capable of optimizing the most well-studied ion acceleration process – rear surface target normal sheath acceleration. Both ribbons and disks are not well-suited for continuous, long-term operation due to limited surface area and debris generation. Additionally, ribbon targets lack the positional stability needed for use with fast-focusing optics.

Liquid targets display substantial benefits to high-repetition-rate operation; the target material can be recycled, they generate little to no debris, but typically require nonnegligible operating pressures (for example, Ref. [68]). Additionally, liquid-based targetry can permit continuous operation as application of the appropriate dual pump scheme permits uninterrupted operation for hours or days.

Liquid sprays or mists have been employed in LPI studies[69], but do not reach the densities required to reflect optical or near-infrared light. Recently, cryogenic hydrogen microjets have demonstrated multi-MeV TNSA of protons at 1 Hz repetition rate[70, 71], but lack precise positional control and require long cool-down times due to cryogenic operation. Liquid crystal films have also exhibited substantial benefits, notably: high-vacuum compatibility due to the low fluid vapor pressure, planar geometry, and

https://doi.org/10.1017/hpl.2019.35 Published online by Cambridge University Press

controllable thicknesses. To date, development of the liquid crystal targets has been performed for few-Hz operation, but further work is required to improve film-to-film thickness repeatability and the capability of repetition rates of 10 Hz or higher[72, 73].

The remainder of this section will present our results for creating various liquid targets using either water or ethylene glycol and operating at 1 kHz. For the purpose of characterization, the presented targets were imaged by probe beam illumination. The laser source used is a Coherent Legend which is frequency doubled to 420 nm and has a full-width at half-maximum (FWHM) pulse duration of 80 fs. The imaging objective is a Mitutoyo Plan APO Infinity Corrected Long Working Distance 10× microscope objective which is projected with an eyepiece lens onto an ImagingSource DMK 42BUC03 CCD. The spatial resolution of the imaging system was approximately 1 μm. Further details on the laser source and imaging systems can be found in Ref. [74].

A set of 1000 images was recorded for each target type. Image analysis was conducted to determine the size, major and minor axis dimensions, and probability of target presence which accounts for both positional and dimensional fluctuations from target to target.

Water, at atmospheric pressure, was used for the target generation and characterization in all cases but that of the liquid sheet target. For this case, we employ ethylene glycol, in a vacuum environment. The liquid microjet system is compatible with a range of fluids, which all function in a similar manner, according to the individual fluid properties. To address the difference between the operation of liquid microjets in air versus in vacuum, other current works have found that the resulting microjet properties do not appreciably differ between the two cases[75, 76].

4.1. Liquid jet targets

The most fundamental and simplistic target to generate with the presented system is that of a liquid jet. Figure 2(A) displays an image of the jet target. Here, a capillary with 30 μm inner diameter was used with water to form a cylindrical jet.

The flow rate from the syringe pump was set to $1\ \mathrm{mL}\cdot\mathrm{min}^{-1}$, which generates a fluid velocity of $23.6\ \mathrm{m}\cdot\mathrm{s}^{-1}$. The corresponding Reynolds number of 795 places the jet well within the limit for laminar flow. The spontaneous breakup length for this condition is 5.76 mm, which allows for laser and diagnostic field of view access to the target interaction region.

As previously mentioned, characterization of the jet was performed with short-pulse, microscope shadowgraphy images. Image analysis was conducted to quantify the size and stability of the jet. We find that the diameter of the liquid jet is 33 μm, with a 1σ standard deviation in the diameter of the jet from shot to shot at less than the 1 μm resolution of the imaging system.

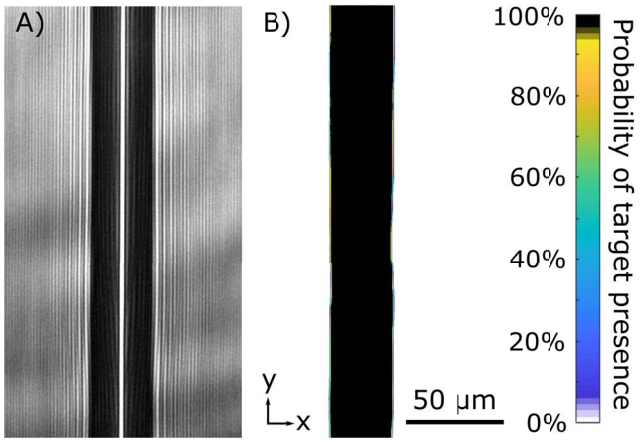

Figure 2. (A) Shadowgraphic microscope image of the liquid jet target. A 30 μm inner diameter capillary generates a 33 μm diameter jet. (B) False-color image of target presence probability. The color scale displays the probability that the target appears in the given location over the 1000 target exposures. Black indicates 100% probability that the target appears in the given location, while white illustrates a 0 probability. The sharp gradient between black and white, shown here, indicates the high positional stability of the liquid jet target.

The positional stability of the jet was assessed by means of the same image analysis routine. From the 1000 images collected, we identify the region of the image where the target is located. We then calculate, on a per-pixel basis, the probability that the target will appear within that pixel over the 1000 recorded instances. We refer to this metric as the probability of target presence – best illustrated by Figure 3.

While this metric does not necessarily quantitatively describe the size, shape, and position of the targets, due to the convolution between these three variables, it does provide an instructive and qualitative indication of the target stability. Note that black indicates that for all 1000 occurrences a portion of the target was located in that position, while white shows where the target does not appear.

The resulting probability of target presence image for the jet target is shown in Figure 2(B). The standard deviations in the position of the left and right edges of the jet are again better than the 1 μm resolution of the imaging system. This stability is attributed to the mechanical stability of the nozzle holder and consistent pressure and flow rate provided by the syringe pump.

With regards to the applicability of the jet target, while not ideal for electron and ion acceleration due to the circular cross-section, this particular target has found use due to the simplicity and straightforward implementation. Initial studies of intense laser–liquid interactions, by Thoss *et al.*, sought to develop sources from a Ga liquid jet with 30 μm diameter irradiated by a 1 kHz repetition rate, 50 fs pulse duration, laser at an intensity of $3\times10^{16}\ \mathrm{W}\cdot\mathrm{cm}^{-2}$[50].

More recent work using the nozzle assembly described in this work has been performed. Backward-moving electron acceleration far exceeding ponderomotive scalings

https://doi.org/10.1017/hpl.2019.35 Published online by Cambridge University Press

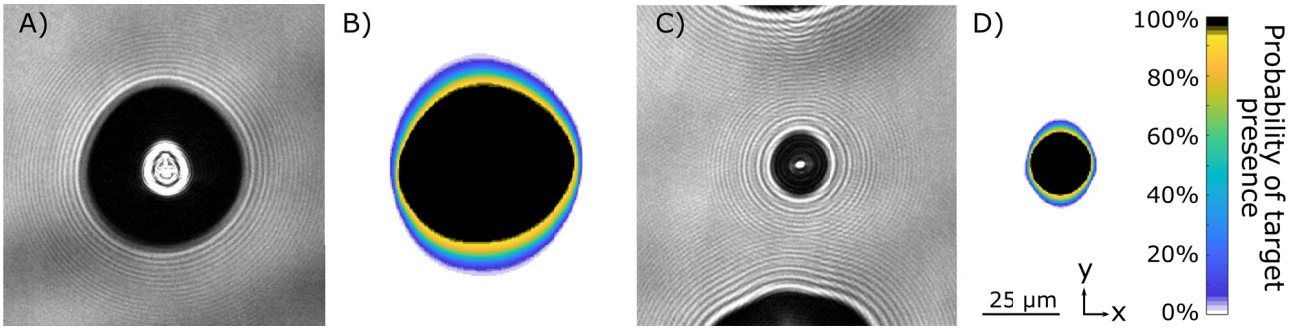

Figure 3. (A), (C) Shadowgraphic microscope images of primary and satellite droplet targets formed by manipulation of the piezoelectric actuator attached to the liquid jet nozzle. The primary droplet in (A) has a diameter of 55 µm and the satellite droplet in (C) has a diameter of 21 µm. (B), (D) False-color images of the probability of target presence for primary and satellite droplet targets. Note that the large gradient, as compared to Figure 2(B), indicates a decrease in the dimensional and positional stability.

at a 1 kHz repetition rate with relativistic intensities was demonstrated[68, 77–79]. These works were performed with water at tens of torr background pressure, though other works have conducted experiments with the use of water jets in vacuum at far lower pressures[80]. Overall, the jet target provides a simple and robust starting point for the presentation of liquid targets for high-intensity LPI experiments and applications.

4.2. Liquid droplet targets

Reduced-mass targets have been explored for their uses in the study of LPI and warm dense matter due to enhanced electron refluxing and heating, resulting from the limitation of return currents which occur in bulk targets[81]. Solid, metal-based reduced-mass targets are relatively expensive and difficult to employ in LPI studies when compared to nonreduced-mass targets. This is due to the added constraints imposed during fabrication of limited transverse dimensions and support of the target by narrow mounting wires.

Liquid droplets are a promising alternative to the solid-based reduced-mass targets that are conventionally used. Prior work has been conducted on ion acceleration and subsequent neutron generation from heavy water droplets[82] synchronized to the laser[83]. In related fields, metal droplet targets are commonly used for EUV and XUV generation, albeit at laser intensities far below the relativistic limit. In this section we present a reduced-mass target based on liquid droplets, which are ideal for high-repetition-rate studies with highly repeatable size and positional control.

As previously addressed, the inherent instability of the liquid jet causes a breakup into droplets after a given distance. This disintegration of the liquid jet is driven by minimization of the surface energy of the fluid and initiated primarily by vibrations and sheer stresses within the liquid jet. Here we intentionally seeded the instability of the jet, via the Plateau–Rayleigh instability, to create droplet formation with high repeatability. This causes the formation of droplets at frequencies greater than 100 kHz with high-precision volume and velocity distributions.

Seeding of the Plateau–Rayleigh instability requires a vibrational or pressure perturbation to be applied to the liquid jet. For this work we seed a vibrational instability with a Thorlabs AE0203D08F piezoelectric actuator which is affixed to the nozzle nut with epoxy as shown in Figure 1. When operated near the spontaneous droplet formation frequency, due to the resonance properties of this effect, a small-amplitude, few-cycle vibration generated by the actuator is sufficient to reinforce instability growth in the liquid microjet.

In high-repetition-rate use, synchronization between the fixed laser pulse frequency of 1 kHz is required in order to have positional stability of the droplet with respect to the laser focus. We employ a 1 kHz trigger signal synchronized to the laser source to time the actuator driver with variable drive frequency, pulse number, pulse duration, delay, and amplitude. While the trigger signal arrives every 1 ms, the actuator driving signal is run in a burst mode with a frequency near that of the spontaneous droplet formation frequency ($f_d = 178$ kHz). Illumination by the shadowgraphy probe pulse, synchronized to the 1 kHz illumination laser source, verifies the timing and stability of droplet formation (Figure 3).

In the process of droplet breakoff, large primary and small satellite droplets are formed in an alternating droplet train which is depicted in Figure 11. For the 30 µm diameter capillary, the large droplet, pictured in Figure 3(A), has a diameter of 55 µm. Formation of the satellite droplets within the droplet train does not occur for all conditions, and is dependent on the viscosity and surface tension of the fluid[61]. For water, used here, satellite droplets shown in Figure 3(C) are formed which alternate with the primary droplets along the propagating droplet train. The satellite droplets are notably smaller than the orifice diameter, at just 21 µm in diameter.

The shape of the primary droplets is slightly ellipsoidal. The major axis length is 56 µm and the minor axis length is

https://doi.org/10.1017/hpl.2019.35 Published online by Cambridge University Press

54 μm. The 1σ standard deviation of the size of these axes is less than ±1 μm from droplet to droplet.

While the dimensional measurements are precisely controlled, the positional stability of the primary droplet target is relatively less well constrained, as illustrated by the probability of target presence map shown in Figure 3(B). For this case, the standard deviation of the centroid position in the horizontal plane, σ_x, is 1.5 μm. In the vertical plane, the centroid standard deviation, σ_y, is 5.7 μm.

The smaller satellite droplet is also slightly ellipsoidal in shape, with a major axis length of 22 μm and minor axis length of 20 μm. The dimensional 1σ values for both axes are less than 1 μm. The centroid positional stability is better constrained for this droplet type. Here σ_x is less than 1 μm and σ_y is 2.4 μm.

The dimensional and positional stability of the droplet targets is critical for use, especially in the case of reduced-mass targets. The droplet targets demonstrated here are well-suited for use with fast-focusing optics, as the positional stability is better than the length of the confocal parameter even for an $f/1$ focusing optic. It may be of interest that generation of droplets of less than five microns is possible using smaller-diameter capillaries and associated additional complications. Further improvements in the droplet positional stability may be made in future versions of the target system which are designed to optimize this parameter.

A number of other approaches to generating droplets have been performed. These methods include pressure-based initiation of the Plateau–Rayleigh instability as opposed to vibrational[84]. Cylindrical piezoelectric actuators which surround the capillary have been shown to be a repeatable method of triggering droplet formation[85]. Even lasers have been used to perturb a liquid microjet and generate repeatable droplet formation[86].

4.3. Liquid sheet targets

Planar, solid density, foils of the order of a few microns in thickness are the most commonly employed target configuration for the study of high-intensity LPI. These foils have proved useful for the study of a wide range of processes, including energetic electron and ion acceleration[1], X-ray generation[87], and even ultra-intense high harmonics[88]. For high-repetition-rate studies and applications, a liquid target with planar geometry and submicron thickness is required.

Literature on the formation of liquid sheets abounds, stemming from a range of fields[89–91]. The requirements which we have outlined, however, have yet to be satisfied. As a result, we build on these other works in order to meet the needs required for use in LPI.

More recently, contemporary efforts to create a flowing, planar, liquid sheet target have resulted in the development of two approaches. First, the method upon which this work is based, is the intersection of two, laminar-flowing liquid microjets. Previous work by Ekimova *et al.* demonstrated the formation of liquid sheet targets as thin as 1.4 μm in vacuum through the head-on intersection of two 50 μm diameter water jets[75]. Our work improves upon this result in two ways: use of nonnormal incidence between the two microjets results in the generation of sheets as thin as 450 nm, while operation with ethylene glycol significantly improves the vacuum compatibility of the system.

The second method is through the use of microengineered nozzles. Galinis *et al.* use 3D printed nozzles with 200 nm resolution to construct a tapered nozzle orifice which is 260 by 30 μm. This forms a sheet as thin as 1.49 μm which is shown to be stable in vacuum and at atmospheric pressure[76]. Another method, by Koralek *et al.*, uses microfluidic gas-dynamic nozzles to produce liquid sheets from 1 μm to 10 nm[92]. This is achieved through pinching of a central microjet by two impinging gas jets.

The nozzle arrangement for this work and the resulting target geometry are illustrated in Figure 4. Through the introduction of a second nozzle assembly, we generate planar, submicron-thick, liquid sheet targets. In the impingement of two equal diameter, equal velocity liquid microjets, a leaf-shaped thin sheet is formed. With the use of 30 μm diameter capillaries and ethylene glycol, the sheet is less than 1 μm thick and displays high dimensional and positional stability. The high-velocity laminar flow additionally makes it suitable for high-repetition-rate use at greater than 10 kHz, as the ablated interaction region is refreshed every 25 μs for the laser conditions used.

To form the sheet, two 30 μm diameter glass capillaries are aligned with the tips in close proximity. The full angle of incidence, $\Delta\theta$, between the two liquid jets is mechanically constrained to be 60°. Unlike other approaches, the jets are intentionally intersected with a grazing incidence where the degree of overlap of the two jets is precisely controlled by means of piezoelectric translation of one capillary with respect to the other. The amount of overlap between the two jets, Δx, ultimately defines the minimum thickness of the sheet. At normal incidence the thickest sheet is formed, typically resulting in a minimum thickness of a few microns. While at grazing incidence configuration, $\Delta x > 0$, a thinner sheet is generated until it is no longer stable, and the lower half of the leaf-like shape does not reconnect at the bottom.

It is important to note that the angle of the sheet relative to the plane of incidence between the two microjets is dependent on Δx, the amount of overlap between the jets. This point is illustrated in Figure 4(C). When the jets are normally incident, the sheet is formed perpendicular to the plane of incidence. However, the thinnest sheet is formed through grazing incidence, where the sheet is clocked to have a $\Delta\phi \approx 15°$ from the plane of incidence. When $\Delta\phi < 15°$ the resulting sheet is unstable, with the lower half of the leaf-like shape open at the bottom.

https://doi.org/10.1017/hpl.2019.35 Published online by Cambridge University Press

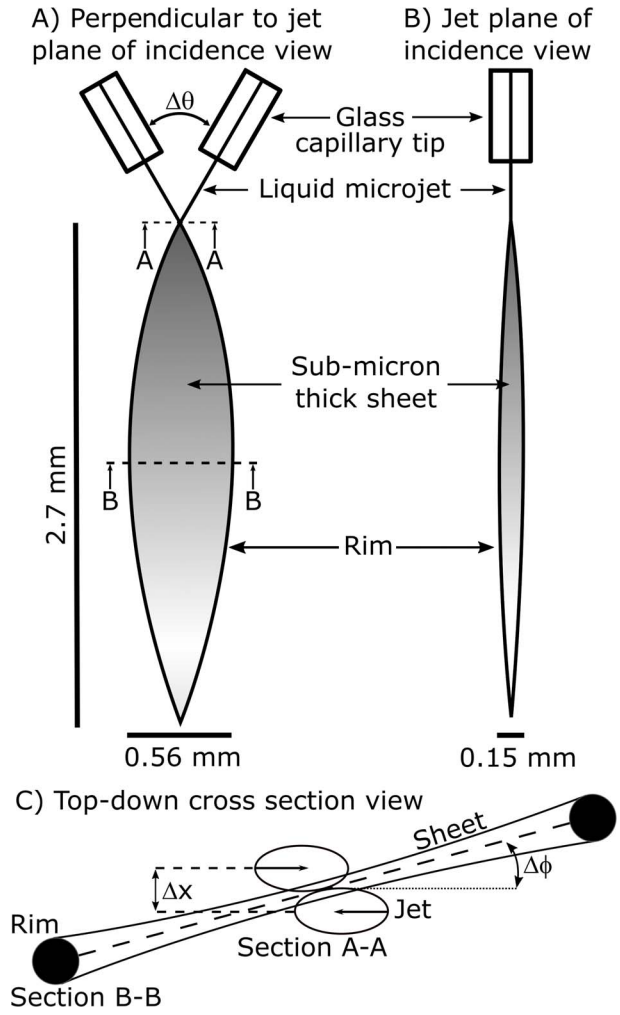

Figure 4. (A) View of capillary nozzles and thin liquid sheet formed perpendicular to the plane of incidence between the jets. The full angle between the two jets is denoted as $\Delta\theta$. (B) View of the sheet formation within the jet plane of incidence. Note that the sheet is not aligned to this plane due to the grazing incidence of the two jets. (C) Top-down cross-section views of the jet intersection and resulting sheet formation. Section A–A illustrates the grazing incidence of the two jets which allows the formation of a submicron-thick sheet. Section B–B shows the relative angle, $\Delta\phi$ of the plane of the sheet with respect to the plane of incidence of the jets. The thick, cylindrical rim which supports the sheet is shown as well.

Following the dual microjet geometry described above, and with the use of ethylene glycol at a 23.6 $m \cdot s^{-1}$ fluid velocity and grazing jet impingement, the sheet formed is shown in Figure 5(A). The dimensions of the sheet are 2.6 mm long by 0.56 mm wide, as measured by microscope imaging. A two-dimensional thickness map of the sheet was measured using a commercial Filmetrics white-light thin film interference device, and is shown in Figure 5(B).

The sheet thickness at the top is a few microns thick. Further down, the sheet thins to a minimum of 450 nm, as denoted by the white cross in Figure 5(B). Progressing toward where the rims reconnect at the bottom of the sheet, the sheet thickness increases again.

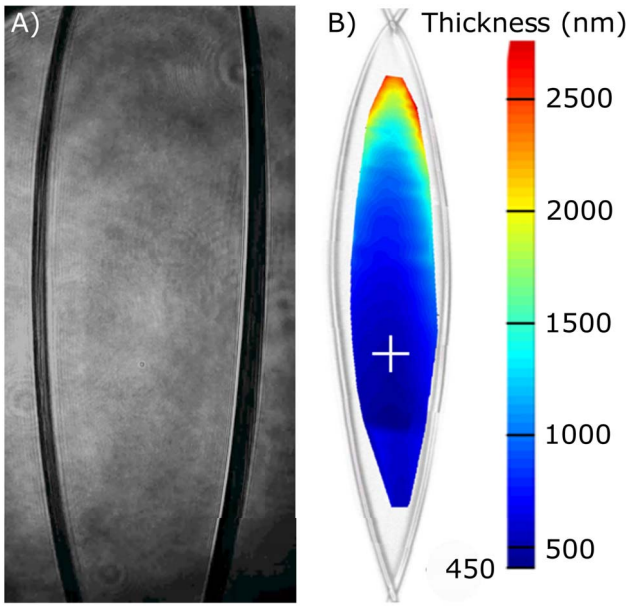

Figure 5. (A) Microscope shadowgraphy image of the central region of the liquid sheet target in vacuum. (B) Spatially dependent thickness map across the liquid sheet, collected with a Filmetrics white-light interference profiler. The white cross indicates the location of the minimum sheet thickness at 450 nm. For scale, the width of the sheet in (B) is 560 μm. This figure is reprinted with permission from Morrison *et al.*[93].

For the above-described configuration, with the use of ethylene glycol, 450 nm was the minimum achievable thickness. It should be noted, however, that we have created sheets with water as thin as 275 nm using the same jet configuration. Unfortunately, these sheets are unstable and the rims do not close at the bottom. Efforts to further reduce the sheet thickness are ongoing.

The structure of the sheet is supported by the two thick, >25 μm diameter jets which do not coalesce into the thin sheet and support the leaf-like shape. As a result, the edges of the sheet are relatively thick compared to the thin film at the center.

Subsequent secondary and higher-order leaf-like structures are formed below the primary sheet. These sheets, however, are relatively thick in comparison to the first sheet, and smaller in length and width. The sheet ultimately disintegrates into a droplet spray after the onset of the Plateau–Rayleigh instability.

Other notable variables of the submicron-thick sheet target include the control of fluid velocity. As the fluid velocity increases, so does the length and width of the sheet. There are, however, practical limitations to the overall size of the sheet as determined by the psi rating of the syringe pump, Reynolds number limit for laminar flow, and the resulting spontaneous breakup length, which is dependent on the flow velocity. Additionally, all of these values ultimately depend on the fluid used.

The sheet target is not depicted in terms of the probability of target presence, as it is not well characterized in terms

https://doi.org/10.1017/hpl.2019.35 Published online by Cambridge University Press

of dimensional and positional stability by this illustration. The critical stability values for the sheet target are instead the target angle, optical axis positioning, and sheet thickness. The target angle stability was measured by means of image analysis from frames collected in the testing of the plasma mirror (see Section 5). Thresholding and centroid identification was performed for the frames collected by the CCD camera from the specular, high-field reflection off the liquid sheet as a plasma mirror. The 1σ standard deviation in the reflected beam position centroid was less than 1 pixel in both x and y. The longitudinal positional stability of the sheet was measured to be better than 2 μm by means of side-on microscope imaging. Lastly, the thickness stability of the sheet was found to be stable to better than 3 nm over a 10 μm patch, as evidenced by the etalon-like thin film interference measurement performed in Section 5.

The above-described submicron-thick, planar liquid sheet target has already been demonstrated for use in high-intensity, high-repetition-rate LPI experiments. Morrison *et al.* employed this target, in combination with a kHz repetition rate, millijoule-class, relativistically intense laser to generate energetic protons at up to 2 MeV at a kHz repetition rate[93]. Previous efforts to accelerate ions at kHz repetition rates have relied on front surface TNSA from relatively thick targets, providing diminished efficiencies compared to rear surface TNSA[94]. This demonstration is a substantial advance toward utilizing the full capability of high-repetition-rate lasers and meeting the needs of promising applications[95].

4.4. Exotic liquid targets

Aside from the relatively simple cylindrical, spherical, and planar geometries formed by the jet, droplets and sheet targets, more exotic and complex geometries are possible. During our efforts we explored a few exotic configurations which may be of interest to the LPI community. These represent only a small subset of possible liquid targets. The results we highlight here are meant to be illustrative, not exhaustive. In this section we present isolated disks, cylindrically curved sheets, and narrow wires a few microns in diameter, as shown in Figure 6.

These targets have a range of potential use cases for both fundamental studies and applications. In particular, the isolated disks function as reduced-mass targets. As previously addressed, reduced-mass, planar targets are of high interest to the high-intensity laser–plasma community for their known role in the enhancement of ion acceleration due to the promotion of enhanced electron refluxing and sheath fields[96, 97]. This results in higher conversion efficiency and peak ion energies for the TNSA ions. The cylindrically curved surface targets enable the potential for control of ion beam divergence. Previous work has demonstrated the use of curved surfaces in LPI experiments as a method to focus ion beams for secondary target heating[98]. Additionally, surface high-harmonic beam focusing could be controlled with such a target, as control of the beam is sensitive to the spatial phase of the target at the point and time of generation[99–101].

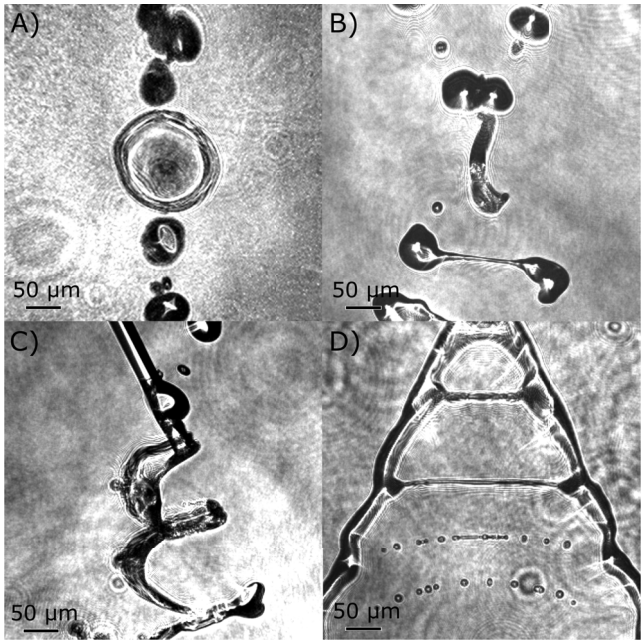

Figure 6. A variety of other unique target configurations can be created with droplets and jets. (A) Face-on view of droplet–droplet collision designed to make an isolated disk target. (B) Side view of the droplet–droplet isolated disk target shown in (A). (C) Droplet–jet collision generating a target with cylindrical surface shape. (D) Thin (≈5 μm diameter) horizontal wire formed through the intersection of two jets while driving the Plateau–Rayleigh instability with a piezoelectric device.

4.4.1. Isolated disk targets

An alternative approach to producing thin planar targets, from the method detailed for the submicron-thick sheet targets, is through the collision of two droplets[102]. To create isolated disks, our two liquid jet nozzles are operated in droplet mode by oscillating the piezoelectric actuator near the spontaneous droplet frequency with a burst frequency of 1 kHz such that the droplet train is synchronized to the imaging probe pulse. One nozzle position was fixed while the other was translated in order to overlap two droplets just after breakoff from the liquid jet. The full angle between the two colliding droplets was 60°. The face-on and side views of the isolated disk target are shown in Figures 6(A) and 6(B). A 130 μm diameter disk is formed with a relatively thick rim with an average diameter of 17 μm. Using volume conservation from the two droplets, along with the thickness of the rim, the thin sheet spanning the center of the isolated disk is approximately 8 μm thick, which is certainly within the desired range for TNSA.

Tuning of the angle normal to the disk surface is performed through off-normal collisions of the two droplets in the horizontal and vertical planes. The off-normal intersection

https://doi.org/10.1017/hpl.2019.35 Published online by Cambridge University Press

serves to rotate and oblate the disk, though global rotation of the two nozzles can maintain the sheet symmetry while also achieving a rotation. Another tuning parameter which can be used to modify the interaction is the evolution time of the droplet collision. This changes the aspect ratio, shape, and general morphology of the droplet collision, and could be exploited to create other unique target types.

Additionally, relative fluid velocity, angle of incidence, and fluid properties such as surface tension and viscosity modify the droplet interaction and the resulting disk size, inner sheet thickness, and subsequent droplet temporal evolution. These parameters have not been surveyed in this work, but are proposed for future studies with relevance to high-intensity LPI targetry.

Droplet-on-demand generators where the droplets are expelled from the capillary orifice only when requested, instead of the continuous droplet generation approach used here, may be applied for droplet–droplet collisions on lower-repetition-rate laser systems or those which have concerns about vacuum pumping rate or excess background gas pressure[103].

4.4.2. Cylindrically curved sheet targets

One method of generating a high-repetition-rate liquid target with a curved surface is through a droplet–jet collision. As shown in Figure 6(C), the droplet–jet collision forms a cylindrically shaped sheet with the primary axis of curvature oriented horizontally. At early times in the interaction, a saddle-shaped feature is formed with curvature along the vertical axis due to the diameter of the droplet (55 μm) being larger than that of the jet (30 μm). The overfill of the interaction streams past the jet until surface tension pulls back the fluid.

Further modification and tailoring of the curved surface target can be performed by varying the relative size of the jet and droplet, angle of incidence, fluid properties, etc. These variations should enable variation in the radius of curvature, thickness, and other relevant parameters of the resulting curved surface.

4.4.3. Narrow wire targets

Here, the piezoelectric actuators are operated continuously near the spontaneous droplet frequency to establish the Plateau–Rayleigh instability. Before droplet breakoff, a modulation in the diameter of the jet is formed resulting from the resonant instability. When two peaks from this modulation are overlapped between the two jets, the collision forms a triangular, ladder-like structure. The horizontally oriented rungs shown in Figure 6(D) are as small as 5 μm in diameter. The length of each rung is over 200 μm, generating a long-aspect-ratio, narrow wire spanning two relatively thick jets.

Proposed uses for these exotic target types are not directly clear, but unique and novel geometries are commonly used in LPI studies to measure, enhance, or modify various parameters[104, 105]. The exotic targets shown here are just a few of the numerous target configurations capable of being made with the liquid microjet assembly. The overall parameter space for liquid targets is far too broad to be addressed in detail in this work, but we hope that these unique configurations stimulate the community to consider the possibilities this technique presents.

5. Liquid optics

Liquid-based optical elements are commonly used in a wide range of optical applications. Dye jet lasers, liquid lenses, and an array of various liquid crystal-based optics, including phase and amplitude modulators, prisms and lenses are now ubiquitous. In many applications, use of fluids instead of more conventional solid-state optics offers performance benefits such as variable focal lengths, electrically addressable control, or consumable modes of operation.

Liquid optics for high-repetition rate, high-intensity LPI also show promise to offer advantages over conventional optics, primarily in cases where the optical element is consumable. Liquids offer the capability for rapid refreshment and low cost per shot, such that use at high repetition rates is viable. By generating the optic on an individual shot-to-shot basis, this avoids the usual concerns that the optics will be damaged by the fluence of the laser pulse. This quality is particularly advantageous when employed in extreme environments, such as those in the vicinity of the LPI.

5.1. Liquid plasma mirror

With the push to develop high-intensity lasers which operate at kHz repetition rates or higher, associated optical devices must also meet these demands. One such class of optical devices aims to improve the temporal pulse contrast of the laser pulse by suppressing or removing prepulses and pedestal features that prematurely damage the target and generate preplasma which can be detrimental to experimental objectives such as high-energy ion acceleration. Many solid-state temporal pulse cleaning devices such as Pockels cells, saturable absorbers, crossed polarized wave generation (XPW), and optical parametric amplifiers (OPAs) have been demonstrated at high repetition rates as well. One commonly employed temporal pulse cleaning technique, plasma mirrors, however, are not ideally suited for high-repetition-rate use due to the consumable nature of the mirror media.

Typically composed of an anti-reflection coating on an optical quality substrate, a plasma mirror maintains low reflectivity until the leading edge of the pulse generates a highly reflective plasma on the surface. This technique nominally results in a contrast enhancement by a factor of 100 at the expense of approximately 25% of the energy. Since the irradiated region of the optic is destroyed on

https://doi.org/10.1017/hpl.2019.35 Published online by Cambridge University Press

each shot, the substrate is rastered, realigned, and ultimately discarded after a series of exposures.

Previous demonstrations of liquid-based plasma mirrors have been performed with the use of ethylene glycol flowing from a dye laser jet[106]. While capable of operating at kHz repetition rates, the system exhibited poor contrast enhancement unless operated at Brewster's angle, where a 400:1 contrast improvement was shown, at the expense of low reflectivity of only 38% due to oblique incidence with p-polarization. Another liquid-based plasma mirror technique is based on laminar fluid flow over circular apertures[107]. This work showed a high reflectivity of 70%, but low contrast enhancement of 35 due to the lack of anti-reflection properties. One of the most promising approaches utilizes variable-thickness, submicron-thick, liquid crystal films to create plasma mirrors[108, 109]. These films exhibit anti-reflection properties due to thin film destructive interference when formed to the appropriate thickness, but they have only been demonstrated at repetition rates up to a few Hz.

As described in the remainder of this section, we expand on these techniques to demonstrate the use of a less than 1 μm thick liquid sheet formed by the intersection of two 30 μm diameter, laminar-flowing liquid microjets of ethylene glycol to create a plasma mirror. The liquid sheet exhibits variable low-field reflectivity between 18.5% and as low as 0.1% due to etalon-like constructive and destructive interference. As a plasma, the reflectivity is 69%, providing a temporal pulse contrast enhancement of 690. The presented liquid plasma mirror is demonstrated at a 1 kHz repetition rate in vacuum with an ambient pressure of less than 1 millitorr.

5.2. Anti-reflection properties of thin liquid sheet

Enhancing contrast with the use of a plasma mirror requires that the optical surface in the low field should exhibit low reflectivity. While solid-state plasma mirrors rely on dielectric coatings to achieve this effect, an alternative solution is to leverage an etalon-like effect of destructive interference in a thin film. The etalon reflectivity, R_{etalon}, for a thin film is given by

$$R_{\text{etalon}} = 1 - \frac{1}{1 + F\sin^2(\Delta/2)}, \tag{1}$$

where

$$\Delta = \frac{4\pi n d \cos\theta_t}{\lambda} \tag{2}$$

and

$$F = \frac{4R_i}{(1-R_i)^2} \tag{3}$$

for index of refraction n, sheet thickness d, internal angle of transmission in the film θ_t, wavelength λ, and polarization-dependent single-interface reflectivity R_i. For this work, we use ethylene glycol, where $n = 1.4263$[110], an external angle of incidence of 35°, which gives $\theta_t = 23.71°$, a central wavelength $\lambda = 790$ nm, and R_i defined for s-polarized light. The resulting etalon reflectivity as a function of film thickness is as shown in Figure 7(A).

Note that the etalon reflectivity is a function of incidence angle and wavelength. By focusing onto the thin film, a range of angles are introduced. To mitigate this effect, we operate near focus, within the Rayleigh range, where the wavefronts are nominally flat. Therefore, we do not consider the angle-dependent reflectivity, and instead focus on the unavoidable wavelength dependence required to support an ultrashort pulse.

A MATLAB script was written to calculate the thickness-dependent etalon reflectivity over the range of wavelengths contained within the pulse spectrum. This reflectivity was

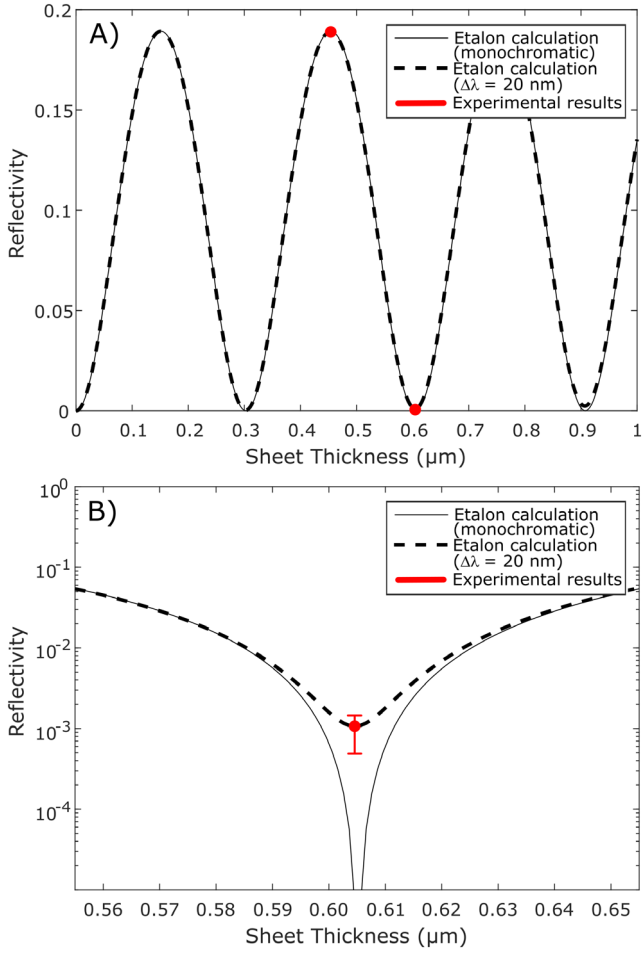

Figure 7. (A) Etalon reflectivity as a function of thickness for the given experimental conditions. The single-wavelength calculation is plotted with a solid line while the wavelength-broadened curve corresponding to a Gaussian FWHM bandwidth of 20 nm is given by the dashed curve. (B) The bandwidth-dependent etalon reflectivity is plotted on a semi-log scale for the third minima to illustrate the effect of incidence with a broad bandwidth laser pulse. Note that while the etalon calculation continues toward zero at the minima for the monochromatic case, the minimum reflectivity for a pulse with 20 nm bandwidth is approximately 0.1%.

https://doi.org/10.1017/hpl.2019.35 Published online by Cambridge University Press

then weighted to the energy contained within each wavelength, and is referred to as the bandwidth-dependent calculation. To match the experimental laser pulse, a spectrum with a Gaussian distribution centered at 790 nm and FWHM $\Delta\lambda = 20$ nm was used for the bandwidth-dependent calculation and is co-plotted with the reflectivity for the monochromatic case in Figures 7(A) and 7(B).

The linear scale plot in Figure 7(A) does not reveal a large discrepancy between the monochromatic etalon calculation and bandwidth-dependent etalon calculation. When plotted on a semi-log scale about the third minima, given by Figure 7(B), the differences are apparent. The monochromatic etalon calculation rapidly declines toward the minima with $R_{\text{etalon}} < 10^{-5}$, while the wavelength-dependent etalon calculation reaches a lower limit of $R_{\text{etalon}} \approx 10^{-3}$.

The bandwidth-dependent etalon reflectivity of the thin film puts a lower limit on the reflectivity at each minima. At higher-order minima, the minimum reflectivity increases. Therefore, operation at the lowest minima possible is desired, which in our case is at 605 nm.

A number of different pulse durations can be used to access the physics of high-intensity laser–plasma interactions. These pulse durations span from few-cycle pulses up to greater than picosecond durations. To consider the minimum reflectivity from an etalon-like destructively interfering sheet for these pulse durations, we examine the Fourier-transform-limited bandwidth for pulses centered at 790 nm with pulse durations of 1 ps, 300 fs, 100 fs, 30 fs and 7 fs. The results of these calculations are summarized in Table 1.

Fitting the results of Table 1 to a function results in the following expression; $R \approx 0.5 \times T^{-2}$, where R is the reflectivity at the first minima, and T is the FWHM pulse duration. As expected, pulses which have narrower bandwidths result in lower minimum reflectivities. However, the shape of the decrease in reflectivity is quite narrow in terms of sheet thickness as it approaches zero, which can be seen for the monochromatic case plotted in Figure 7. Therefore, in order to achieve this calculated minimal reflectivity, the tolerance for variation in thickness of the sheet must be minimized over the spot size of the laser.

It should be noted that the effect of spectral phase was ignored for the calculation of the etalon-like reflectivity because we consider only a single pulse case. For configurations where double or multiple pulses are incident onto the sheet in the low field, spectral interference between the two pulses can impact the ultimate reflectivity and pulse contrast enhancement.

Table 1. Pulse durations, Fourier-transform-limited bandwidth, and calculated minimum reflectivity for reflection from an etalon-like thin film at the first destructive minima.

FWHM pulse duration (fs)	FWHM bandwidth (nm)	Minimum reflectivity
7	134.5	1.06×10^{-2}
30	31.38	6.14×10^{-4}
100	9.41	5.54×10^{-5}
300	3.14	6.18×10^{-6}
1000	0.94	5.62×10^{-7}

5.3. Experimental setup and results

The thin, liquid sheet was experimentally tested for its anti-reflection properties and its use as a plasma mirror. A few hundred thousand shots were taken with s-polarized light at low intensity ($I < 10^{11}$ W $\cdot$ cm^{-2}) to measure the reflectivity of the sheet in the low-field case. A schematic of the experimental setup is shown in Figure 8. A 25.4 mm diameter, 152.4 mm focal length protected gold-coated off-axis parabolic mirror with an off-axis angle of 90° was used to focus pulses with a 15 mm input diameter, 50 μJ energy, and chirped to 200 ps pulse duration at a 1 kHz repetition rate, onto the sheet at an angle of incidence of 35°. The focal spot size at the sheet was measured to be 7.8 μm by 12.1 μm, resulting in an intensity of approximately 7.6×10^{10} W $\cdot$ cm^{-2}. Pump–probe shadowgraphy was used to confirm that the sheet was unperturbed by the laser pulse in the low field. All tests for the plasma mirror were performed under vacuum at a chamber pressure below 1 millitorr.

In addition to temporal pulse contrast enhancement, plasma mirrors can exhibit spatial mode cleaning properties. When operated near the focus, as in this case, the higher-order spatial modes are effectively filtered out of the reflected beam because the intensity-dependent reflectivity is less in these regions. This effect was recorded in the high-field case with the input and reflected laser modes in the near-field, as shown in Figure 9. These images were collected from a single shot while operating at a 1 kHz repetition rate. Figure 9(A) exhibits many hard edges and diffractive features common in high-intensity laser modes; the mode reflected from the plasma mirror, as shown in Figure 9(B),

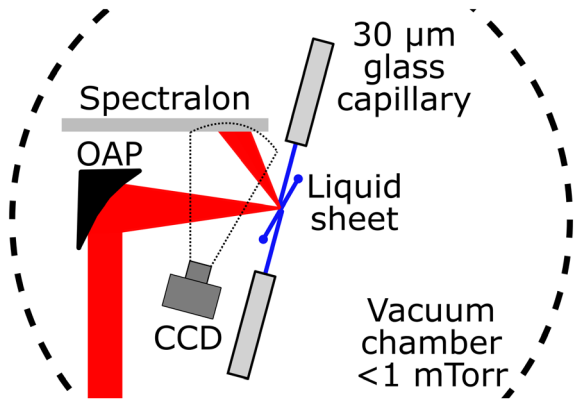

Figure 8. Experimental setup for measuring the thin, liquid sheet plasma mirror reflectivity. The laser was focused onto the liquid sheet at a 35° angle of incidence. The reflected light was then scattered by a Spectralon panel, which was imaged by a CCD. While operating at a 1 kHz repetition rate, the vacuum chamber pressure was maintained below 1 millitorr.

https://doi.org/10.1017/hpl.2019.35 Published online by Cambridge University Press

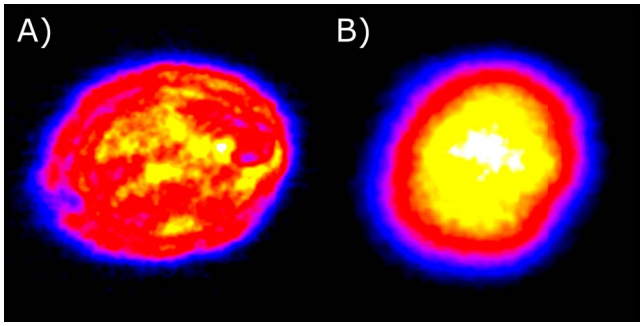

Figure 9. (A) Near-field mode of laser pulse input onto the plasma mirror. (B) Near-field mode of laser pulse after reflection from the plasma mirror. Note the smoothing of the mode performed by the plasma mirror.

smooths out these hard edge features, resulting in a smoother mode quality.

The reflectivity was recorded by means of an Imaging-Source DMK23UP1300 CCD imaging a Spectralon panel. Calibrated filters were placed in front of the CCD and the camera integration time was changed to enable the high-dynamic-range measurement. Absolute calibration for the high- and low-field measurements was performed by placing a protected silver mirror out of focus and reflecting the light directly onto the Spectralon panel.

Since the thickness of the sheet varies most drastically along its vertical length, from 500 nm to greater than 1 μm, the sheet was rastered vertically while observing the reflected light. In this way, the constructive and destructive interference maxima and minima were surveyed and recorded. We observe a constructive interference maximum reflectivity in the low field of 18.5%, which is the mean reflectivity calculated from the collection of 1000 individual laser–target interactions. The CCD exposure time for this case was such that only a single laser pulse was collected per frame. In the destructive interference case a mean minimum reflectivity of $0.1\% \pm 0.05\%$ was determined from recording 1000 frames, where each frame integrated 250 laser–target interactions. Multi-shot integration by the CCD was necessary due to the low energy per pulse used and low reflectivity. Accuracy of the measurement in the low field was limited by the amount of scattered light from the focusing optic, which reflected from the liquid sheet then onto the Spectralon panel in the vicinity of the reflected spot. The experimental error resulting from this effect was thus calculated to be $\pm 0.05\%$.

These results are consistent with the constructive maxima shown in Figure 7. The destructive minima was found to be congruous with the broad-bandwidth etalon reflectivity calculation at the third reflectivity minima with a sheet thickness of 605 nm. Though the sheet thickness was not measured *in situ*, the estimated value is well within the range of values provided by previous measurements performed with a Filmetrics commercial thin film interferometric measurement device.

Following the same procedure, the high-field reflectivity was recorded with the same experimental setup, but with 1.3 mJ of energy per pulse and a 50 fs Gaussian FWHM pulse duration, as measured by a single shot autocorrelator, for an on-target intensity of 8.8×10^{15} W · cm^{-2}. For these experimental conditions, a high-field reflectivity of 69% was recorded. This value is in agreement with other results from the literature for both solid-state and liquid-based plasma mirrors[111–113]. Incorporating the low-field reflectivity of 0.1% with the high-field reflectivity of 69%, the contrast enhancement factor for this configuration is 690.

The pointing stability of the reflected pulse from the plasma mirror in the high field, as shown in Figure 9(B), was also analyzed using a MATLAB script. This analysis showed that the standard deviation of the centroid in reflection for the high-field case was 130 μrad in the vertical axis and 250 μrad in the horizontal axis. The input pointing stability of the laser pulse is unresolvable with our current focal spot imaging techniques, whereby using a 30 mm focal length, $f/1$ optic we observe less than 1 μm jitter in the focal plane.

5.4. Discussion of experimental results

Here, we have demonstrated, to our knowledge, the first liquid-based plasma mirror with etalon-like anti-reflection properties, capable of operating at repetition rates exceeding 1 kHz. The temporal contrast enhancement of 690 is comparable to, or exceeds, results reported for both solid-state and liquid-based plasma mirrors operating at substantially lower repetition rates. This technique is highly stable and, with two high-pressure syringe pumps, can be operated indefinitely.

These results, however, are not without drawbacks, which may limit the applicability of the described plasma mirror. The usable area on the plasma mirror, over which the low-field reflectivity is minimized and the sheet is locally flat, is approximately 30 μm in diameter. Since the high-field reflectivity is a function of intensity, which peaks around 1×10^{16} W · cm^{-2}, the optimal incident energy for a 30 fs pulse is only 2 mJ[111, 114]. Use with more energetic pulses over this region would result in lower reflectivity and similar contrast enhancement. Alternatively, larger focal spot sizes would result in a reduced average low-field reflectivity and spatially dependent contrast enhancement, due to the varying thickness of the sheet over the focal spot size. However, longer pulse durations with narrower Fourier-transform-limited bandwidths would permit use with more energy per pulse, as the intensity would be lower and also benefit from lower low-field reflectivity, as presented in Table 1.

Operation of the plasma mirror at the third etalon minima also limits the bandwidth-dependent low-field reflectivity. The ideal operational thickness condition is at the minima, centered around 300 nm. This lower minima permits a broader wavelength tolerance and lower low-field reflectivity over a larger range of sheet thicknesses.

https://doi.org/10.1017/hpl.2019.35 Published online by Cambridge University Press

To be clear, there are advantages and disadvantages to the use of a conventional anti-reflection-coated dielectric plasma mirror as compared to the liquid-based approach described here. Dielectric plasma mirrors afford the user a large and variable surface area to irradiate. This enables tuning of the intensity at the plasma mirror surface for optimization of high-field reflectivity, nearly independent of the pulse duration and energy used. The low-field reflectivity for these devices is well characterized and designed to match the laser wavelength, bandwidth, and angle of incidence. In optimized conditions, contrast enhancements of up to 10^4 are achievable[115]. Anti-reflection dielectric plasma mirrors are inherently vacuum-compatible and are commonly employed at many facilities, resulting in straightforward implementation if required. Disadvantages of these solid-state optics include: relatively high cost per shot, significant debris generation, and technical difficulty in implementing this technique at high repetition rates.

The liquid-microjet-based plasma mirror device described here is advantageous for its low cost per shot, low to no debris generation, and high-repetition-rate usability. However, due to the limited area at which the sheet is at or near the destructive minima, the maximal pulse energy is somewhat limited by the optimal intensity for maximum reflectivity. Other disadvantages include difficulty in implementation of the microjet system in a vacuum environment, which may require significant alteration of the vacuum system.

Nonetheless, the results presented here establish a proof-of-principle demonstration of one such optical element commonly used in low-repetition-rate LPI studies, but now through the adoption of a fluid media, adaptable for use in high-repetition-rate operation. Future developments in the creation of submicron-thick liquid sheets will serve to further improve the range of laser parameters under which this type of device can be of use. Additionally, we hope to see the invention of other complementary liquid-based optical elements, such as the aforementioned plasma focusing optics.

6. Practical considerations

As previously mentioned, we use ethylene glycol in the experiments presented in this paper. By commenting on desirable properties of liquids for these experiments and other constraints, this section provides some justification of this choice and other considerations for using other liquids for experiments of this kind. As will be discussed, for experiments requiring a vacuum environment, selecting a liquid with a low vapor pressure is important, and there are other concerns for the design of the vacuum pump system to be considered; however, for experiments that do not require vacuum conditions, a wider range of liquids can be employed (for example, Ref. [68]). We also briefly address the gas density of vapor surrounding these liquid targets in vacuum, which can cause significant consequences in terms of ion acceleration, electron acceleration, and surface harmonic generation[79, 93, 116].

As we anticipate the development of relativistically intense laser systems with repetition rates of kHz or higher, we estimate the maximum potential repetition rate for the cylindrical jet, droplet, and sheet targets. This measurement is performed by use of pump–probe shadowgraphy with high temporal resolution over microsecond time delays. With this technique, we determine the time required to reestablish a new target in the interaction region and infer the potential for use at repetition rates in excess of 1 kHz.

6.1. Vacuum operation with liquid microjets

In the experimental study of high-intensity LPI, vacuum operation is necessary in order to prevent nonlinear effects from degrading beam quality during propagation to the target[117–119], neutralization of ion acceleration[93], and to enable the use of electrostatic diagnostics such as a Thomson parabolic spectrometer[120]. Vacuum operation with the described liquid target system requires a two-pronged approach. First and foremost is the use of the appropriate fluid with relatively low vapor pressure, with the added complication of debris-free operation. Second is the efficient extraction or containment of excess liquid from the primary vacuum chamber where the laser–target interaction occurs.

While the liquid target system is compatible with a number of fluids, those with low vapor pressure are ideal for low-vacuum operation. Counter to this point is the added constraint of relatively low viscosity. In practical application, the fluid viscosity is limited only by the available pump pressure. Due to the choked flow nature of the long-aspect-ratio glass capillary orifices, the bias pressure required for flow is increased as compared to less restrictive nozzles. Use of scanning electron microscope apertures or tapered nozzles reduces this constraint, and enables the use of higher-viscosity and lower-vapor-pressure fluids for the same bias pressure.

Another important fluid characteristic to consider is debris-free operation. The amount of debris generated with high-repetition-rate lasers, as compared to the low-repetition-rate systems currently used, is substantially increased. Metal-based targets, when used with low-repetition-rate systems, typically rely on the low number of laser shots or thin pellicles in order to avoid appreciable accumulation of ablated material from deteriorating or damaging sensitive optics and diagnostics. Liquid metals present low vapor pressures, but produce debris accumulation within the vacuum environment, rendering them unsuitable for high-intensity, high-repetition-rate work[121, 122].

Use of the appropriate debris-free fluid, where excess target material is evacuated from the chamber as gas load on the vacuum pumps, significantly aids operation. Further,

https://doi.org/10.1017/hpl.2019.35 Published online by Cambridge University Press

cleanup is expedited and removal of target material build-up on delicate optics is rendered unnecessary.

In our work to improve vacuum levels during liquid sheet target operation, we learned fluid containment and extraction in the form of a proper fluid catcher design is crucial. Initial efforts to improve liquid collection and vacuum isolation of the main chamber from the fluid catch chamber used small-aperture orifices. As the syringe pump is brought to pressure, droplets fall from the glass capillaries into the orifice, forming a meniscus. Once brought to pressure, the liquid microjet does not produce enough pressure to blow out the meniscus, and instead causes entrainment[123, 124]. The bubbles coalesce, expand, and sputter fluid back into the main vacuum chamber, disturbing the liquid sheet and raising the background chamber pressure.

Bubbling at the catch orifice was resolved by utilizing a relatively large, 4 mm diameter orifice where the initial droplets fell through the aperture and did not form a meniscus. A slide was placed in the catcher below the orifice to intercept and guide the microjet stream further into the catch tube. Without the slide, uncontrolled splashing rapidly increases the available surface area for evaporation. This results in increased gas pressure within the catch tube, generating a backflow of gas near the orifice, disturbing the sheet stability.

The complete vacuum system used in this work is illustrated in Figure 10. Here, the liquid supply is maintained at atmospheric pressure before filling the syringe pump 100 mL reservoir. Swagelok lines, with 1/16 inch outer diameter, then route the fluid, under pressure, from the syringe pump to the nozzle assembly. Once the fluid is expelled from the capillary, it is recollected by the catcher orifice and slide, where it is redirected to a differentially pumped liquid reservoir. The pressure in the reservoir can be controlled through the valves to the turbo pump and roughing line.

With the above-described catcher orifice and slide implemented, a base pressure of 500 microtorr was achieved with a 2 mL $\cdot$ min^{-1} flow rate of ethylene glycol in the vacuum chamber. Without the presence of liquid in the vacuum chamber the ultimate base pressure was 40 microtorr. For reference, the turbo pump on the main vacuum chamber provides a pumping rate of 2100 L $\cdot$ s^{-1}. When the thin, liquid sheet is incident with a relativistically intense laser pulse at kHz repetition rates, the vacuum chamber pressure increases to 800 microtorr. Therefore, the increase in vacuum pressure, accounted to the presence of flowing liquid in the chamber, is of the order of that added by the ablation of target material by the presence of the kHz-repetition-rate laser. After this initial increase in pressure, the vacuum pressure is stable and operates continuously. Unfortunately, the vacuum pressure dependences on target shape and laser intensity were not directly investigated in this work, and remain an open point of interest.

There is a threshold where the amount of ablated material from the laser–matter interaction cannot be effectively removed from the vacuum chamber. As a result,

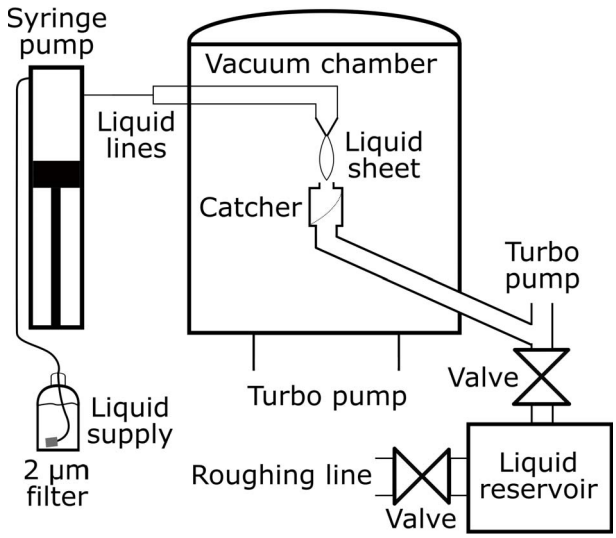

Figure 10. Schematic of vacuum and fluid containment system employed in this work. The syringe pump is fed by a liquid supply at atmospheric pressure. The supply line is capped with a 2 µm sintered steel filter to prevent debris from entering the system. 1/16 inch Swagelok lines and fittings are used to route the fluid into the vacuum chamber, where the two nozzles generate the liquid sheet. A catcher and slide, designed to reduce gas backflow and splatter, direct the residual fluid to the liquid reservoir. Here the excess is isolated from the main vacuum chamber by a turbomolecular pump. The reservoir is kept at relatively low vacuum pressure (≈100 millitorr) through backing with a roughing line. Liquid from the reservoir can be recovered and reused in the system.

the chamber pressure increases above the ultimate base pressure, as in the case presented above. This resulting vacuum pressure may be too high to operate high-voltage-biased diagnostics such as Thomson parabolic spectrometers or to avoid nonlinear optical effects from impacting beam quality. Efforts to further improve the vacuum compatibility of the fluid or configuration of the liquid containment system are ineffective methods to decrease the ambient pressure under these circumstances, since the ablated material from the LPI is the primary degrading cause.

Instead, one must deal directly with the amount of ablated material created. Some proposed methods to address this issue are: decreasing the laser power through a reduction in pulse energy or repetition rate, increasing the pumping rate, or implementing reduced-mass targets. The first approach works in direct competition to the desired high-repetition-rate, high-average-power operation of these laser systems. Increasing the pumping rate on the vacuum chamber is relatively straightforward, albeit somewhat costly. Use of reduced-mass targets may present the most promising approach, in that it directly limits the potential amount of ablated material.

Associated with the impact of background gas density of the vacuum chamber is the preplasma density gradient, which can significantly impact electron and ion acceleration as well as surface harmonic generation[79, 93, 116]. For liquid targets, this is of particular concern due to the evaporation

https://doi.org/10.1017/hpl.2019.35 Published online by Cambridge University Press

of target material and resulting gas density surrounding the target which the laser traverses on the way to the liquid density target surface. The evaporated gas density surrounding the target is impacted by the liquid vapor pressure, evaporated molecular mean free path, and the source size and shape. In short, as the liquid freely propagates through vacuum, molecules on the surface evaporate and cool the remaining target in its liquid state. The gas density at the liquid surface is determined primarily by the local, temperature-dependent vapor pressure. It should be noted here that the vapor pressures for water and ethylene glycol, the two fluids used in this work, at room temperature are approximately 20 torr and 50 mtorr respectively. These values set the order of magnitude scale as an upper bound for the gas density surrounding the liquid target surface.

Behavior of the evaporated molecules can then be characterized by the Knudsen number, K_n, where $K_n = \lambda/L$, with λ as the mean free path and L the characteristic length of the evaporating source[125]. When $K_n < 1$ the molecules are collisional and likely to backscatter to the liquid surface. This condition results in a higher gas density at the surface interface, which shields and insulates the target from further evaporative cooling. With $K_n > 1$ the molecules are kinetic and freely stream away from the liquid target surface, providing a longer scale length of gas density.

Heissler *et al.* derived the background gas density for use with water and ethylene in a cylindrical microjet configuration propagating through vacuum at varying initial temperature[116]. They noted that when $K_n < 1$ the molecules are collisional and provide a vapor shielding effect which was found to be detrimental to harmonic generation as it absorbs XUV light. However, cooling of the liquid or employing other fluids which permit longer mean free paths of the evaporating molecules eliminated the adverse effect of suppressed harmonics.

In the case of ion acceleration with an ethylene glycol sheet target, Morrison *et al.* found that a vacuum chamber pressure above 1 torr significantly decreased the TNSA ion peak energy and number[93]. Of primary concern is the presence of enough electrons in the vicinity of the laser–target interaction to effectively cancel out the space-charge fields required for ion acceleration. They found, below 1 torr, that the peak ion energy and number increased as the background pressure was decreased to 0.1 torr. Below 0.1 torr, the improvements to ion acceleration were negligible.

Aside from the presence of low-density gas surrounding the liquid target surface, which even for the case of water is orders of magnitude below critical density, the liquid targets behave similarly to their solid counterparts in terms of preplasma formation. Prepulses which are intense enough to ionize the target surface will ablate away target material and generate a similar preplasma with comparable scale lengths to those from solid targets. Experimental evidence has shown that liquid targets can successfully be used for surface high-harmonic generation and electron and ion acceleration[79, 93, 116].

The issues presented here, and many other unforeseen issues of practical application, will have to be addressed to move forward with high-repetition-rate LPI studies.

6.2. Repetition rate capability

A practical consideration for application is the maximum possible repetition rate that these targets can support. In order to address this, pump–probe shadowgraphy was used to image the time evolution of the target geometry, along with the appearance of target debris in the region surrounding the laser–target interaction out to the 100 μs timescale. This evaluation is largely qualitative due to the lack of a relativistically intense laser with repetition rates exceeding 1 kHz. Nonetheless, we are unable to posit any deleterious effects which may occur at higher repetition rates, aside from vacuum pressure deterioration due to additional material vaporization, which is discussed in Section 6.1.

The following analysis is illustrated in the frames shown in Figure 11. The laser parameters used here are an intensity of 3×10^{18} W · cm^{-2}, a pulse duration of 40 fs, and a pulse energy of 5 mJ. First, we assess the cylindrical column target formed by a single microjet shown in Figures 11(A)–11(D). The initial liquid column is ablated by the laser pulse, which vaporizes the region surrounding the laser–target interaction. This ablated target material forms a discontinuity in the microjet 1 μs after the interaction, which extends over 100 μm. After 10 μs the microjet has propagated downward and an inverted umbrella-like shape forms which generates a spray of droplets obscuring a subsequent cleanly interacting with the column. By +100 μs, the fluid has propagated sufficiently downward to avoid this droplet spray and presents a new target for the subsequent laser pulse to interact with. This indicates a potential for 10 kHz operation; a value within an order of magnitude of that found by Stan *et al.* using X-ray pulses[80].

The time evolution of the large primary droplet type is shown in Figures 11(E)–11(H).

Approximately 1 μs after the laser pulse deposits its energy, the droplet is still hydrodynamically expanding. Adequate time for the ablated material to evacuate the laser focus region is required. This restricts the repetition rate capability of the droplets to only one out of every ten droplets from the greater than 100 kHz droplet train. By +48 μs, this debris has dissipated from the laser–target interaction region and a second droplet is ready to be shot. One can estimate the droplet targets are capable of operating at a repetition rate of up to 20 kHz.

Lastly, we evaluated the sheet target as shown in Figures 11(I)–11(L). In this geometry the umbrella-like spray from the column target, as shown in Figure 11(C), does not form. Instead, only the thin central region of the sheet

https://doi.org/10.1017/hpl.2019.35 Published online by Cambridge University Press

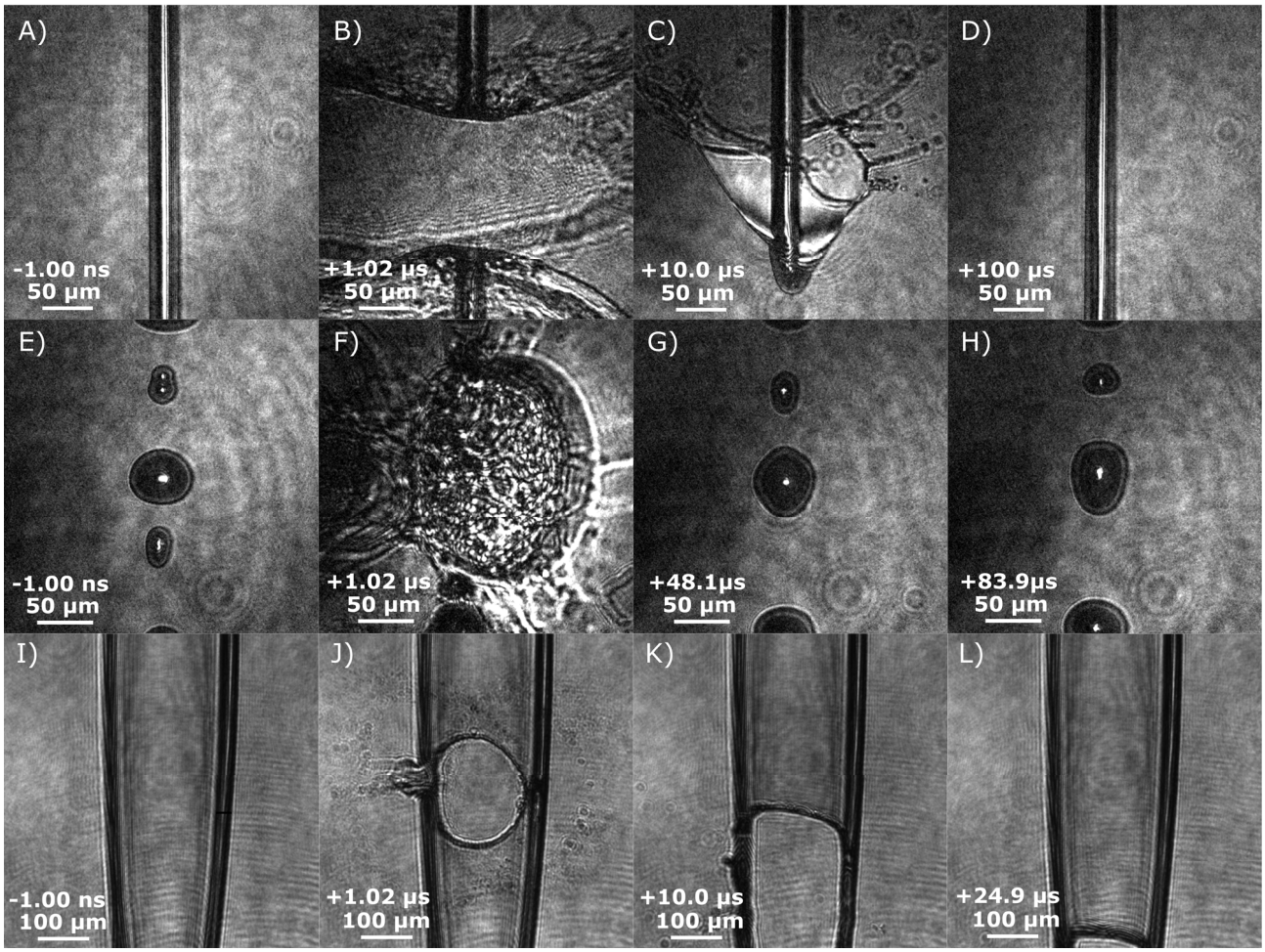

Figure 11. Short-pulse (80 fs) shadowgraphic microscope images of the hydrodynamic evolution before and after irradiation with a high-intensity (10^{18} W/cm^2) laser pulse for liquid (A)–(D) column, (E)–(H) droplet and (I)–(L) sheet targets. These images illustrate the modes of target deformation and prescribe feasible repetition rates for each type. (A) The liquid column begins as a continuous jet which is broken where the laser is incident, as shown in (B). (C) 10 μs after the laser arrives, the column is reestablished, while a conical sheet and droplet spray obscure the laser line of sight. (D) After 100 μs the droplet spray is cleared and a new column is set. (E) A continuous train of primary and satellite droplets are shown before the laser arrives. (F) Hydrodynamic explosion of the primary droplet destroys neighboring droplets within the series. In (G) and (H), separate primary droplets propagate into the appropriate position for subsequent laser shots after 48.1 and 83.9 μs. (I) Two colliding liquid jets form a thin, flowing sheet. (J) 1 μs after the laser–target interaction a circular hole is vaporized. (K) After 10 μs liquid flow begins to reform the sheet and (L) at 24.9 μs the target surface is fully reformed.

must be reestablished. The continuity of the rim supports is illustrated by Figure 11(K). After 25 μs, the central, thin region of the sheet has propagated past the laser–target interaction spot, resulting in a clear target for the following laser pulse. Thus, we conclude that the sheet target is suitable for a nearly 40 kHz repetition rate for these laser conditions.

One practical point of discussion with regards to the repetition rate capabilities is that of scaling with pulse energy. As the pulse energy increases, the amount of material which is ablated and the resulting damage spot both increase. We expect that for joule-class lasers the repetition rate capabilities of these target types will be lower than the few millijoule case which we present. In 1 ms the fluid will propagate 2 cm, which is nearly an order of magnitude above the extent of the damage expected from joule-class lasers[126]. While 40 kHz operation with a joule-class laser may not be feasible, we certainly expect it to be appropriate for 1 kHz operation.

7. Conclusion

We have described the use of fluids, based on high-velocity, laminar-flowing, liquid microjets, as targets and optics for the application and study of high-intensity laser–plasma interactions at $\geqslant$ kHz repetition rate. Formed at room temperature by a robust and simple nozzle assembly, we configure the microjets to create cylindrical jets, droplets, submicron-thick sheets, and several other unique targets. Short-pulse shadowgraphy is used to characterize the targets and to illustrate their dimensional and positional stability.

https://doi.org/10.1017/hpl.2019.35 Published online by Cambridge University Press

Complementary to this effort, we demonstrate a consumable, liquid optical element in the form of a plasma mirror capable of operation at kHz repetition rates. The mirror provides etalon-like thin film destructive interference with 0.1% reflectivity for low optical intensities. At high intensities, where the mirror is in the plasma phase, this configuration produced 69% reflectivity.

We discussed the practical implementation of either target or plasma mirror, including the compatibility of various microjet fluids with in-vacuum operation below 1 millitorr. Lastly, we illustrated through pump–probe shadowgraphy the repetition rate capabilities which exceed 10 kHz.

The above-described targets and optics can be implemented in a wide range of future studies with scope beyond the field of high-intensity laser–plasma interactions. The self-refreshing nature of the targets would present them as ideal for destructive or consumable operation in studies of high-harmonic generation[127–131], shock dynamics[132–134], and X-ray free electron laser irradiation[135–137]. The submicron thickness of the sheet target configuration would suggest its use in research of soft X-ray spectroscopy[138–140], interfacial and surface chemistry[141], and even positron scattering[142, 143]. Future research and development of liquid-based, vacuum-compatible targets and optics will increase the already numerous potential applications.

The flowing-liquid targets and optics we presented are two pieces of a new, high-repetition-rate mode of operation for research involving high-intensity laser–plasma interactions – a mode of operation meeting new demands from the development, construction, and availability of high-repetition-rate, relativistically intense lasers. Flowing-liquid targets and optics scale well to very high repetition rates, while providing densities higher than gas-based targets. Compared with using solids for the same purpose, flowing liquids present a large debris-free, vacuum-compatible, and self-refreshing alternative. This enables relativistic LPI to generate quasi-continuous, high-average-flux sources of electrons, ions, X-rays, and neutrons for use in future application. For these reasons, we encourage the community to adopt this technique to move forward to new and exciting applications.

Acknowledgements

This research is supported by the Air Force Office of Scientific Research under LRIR Project 17RQCOR504 under the management of Dr. Riq Parra. Support was also provided by the AFOSR summer faculty program.

References

1. P. H. Stephen, C. G. Brown, T. E. Cowan, E. A. Henry, J. S. Johnson, M. H. Key, J. A. Koch, A. Bruce Langdon, B. F. Lasinski, R. W. Lee, A. J. Mackinnon, D. M. Pennington, M. D. Perry, T. W. Phillips, M. Roth, C. T. Sangster, M. S. Singh, R. A. Snavely, M. A. Stoyer, S. C. Wilks, and K. Yasuike, Phys. Plasmas **7**, 2076 (2000).
2. R. A. Snavely, M. H. Key, S. P. Hatchett, T. E. Cowan, M. Roth, T. W. Phillips, M. A. Stoyer, E. A. Henry, T. C. Sangster, M. S. Singh, S. C. Wilks, A. MacKinnon, A. Offenberger, D. M. Pennington, K. Yasuike, A. B. Langdon, B. F. Lasinski, J. Johnson, M. D. Perry, and E. M. Campbell, Phys. Rev. Lett. **85**, 2945 (2000).
3. T. Esirkepov, M. Borghesi, S. V. Bulanov, G. Mourou, and T. Tajima, Phys. Rev. Lett. **92**, 175003 (2004).
4. S. Kar, M. Borghesi, S. V. Bulanov, M. H. Key, T. V. Liseykina, A. Macchi, A. J. Mackinnon, P. K. Patel, L. Romagnani, A. Schiavi, and O. Willi, Phys. Rev. Lett. **100**, 225004 (2008).
5. L. Yin, B. J. Albright, B. M. Hegelich, K. J. Bowers, K. A. Flippo, T. J. T. Kwan, and J. C. Fernández, Phys. Plasmas **14**, 056706 (2007).
6. P. Kaw and J. Dawson, Phys. Fluids **13**, 472 (1970).
7. P. Sprangle, C. Tang, and E. Esarey, IEEE Trans. Plasma Sci. **15**, 145 (1987).
8. S. Guerin, P. Mora, J. C. Adam, A. Héron, and G. Laval, Phys. Plasmas **3**, 2693 (1996).
9. G. M. Petrov and J. Davis, Appl. Phys. B **96**, 773 (2009).
10. T. Bartal, M. E. Foord, C. Bellei, M. H. Key, K. A. Flippo, S. A. Gaillard, D. T. Offermann, P. K. Patel, L. C. Jarrott, D. P. Higginson, M. Roth, A. Otten, D. Kraus, R. B. Stephens, H. S. McLean, E. M. Giraldez, M. S. Wei, D. C. Gautier, and F. N. Beg, Nat. Phys. **8**, 139 (2012).
11. T. Ceccotti, A. Lévy, H. Popescu, F. Réau, P. dfıOliveira, P. Monot, J. P. Geindre, E. Lefebvre, and P. Martin, Phys. Rev. Lett. **99**, 185002 (2007).
12. H. Schwoerer, S. Pfotenhauer, O. Jäckel, K.-U. Amthor, B. Liesfeld, W. Ziegler, R. Sauerbrey, K. W. D. Ledingham, and T. Esirkepov, Nature **439**, 445 (2006).
13. S. P. Gordon, T. Donnelly, A. Sullivan, H. Hamster, and R. W. Falcone, Opt. Lett. **19**, 484 (1994).
14. S. Jiang, L. L. Ji, H. Audesirk, K. M. George, J. Snyder, A. Krygier, P. Poole, C. Willis, R. Daskalova, E. Chowdhury, N. S. Lewis, D. W. Schumacher, A. Pukhov, R. R. Freeman, and K. U. Akli, Phys. Rev. Lett. **116**, 085002 (2016).
15. S. Jiang, A. G. Krygier, D. W. Schumacher, K. U. Akli, and R. R. Freeman, Eur. Phys. J. D **68**, 283 (2014).
16. A. Pak, S. Kerr, N. Lemos, A. Link, P. Patel, F. Albert, L. Divol, B. B. Pollock, D. Haberberger, D. Froula, M. Gauthier, S. H. Glenzer, A. Longman, L. Manzoor, R. Fedosejevs, S. Tochitsky, C. Joshi, and F. Fiuza, Phys. Rev. Accel. Beams **21**, 103401 (2018).
17. A. J. Mackinnon, M. Borghesi, S. Hatchett, M. H. Key, P. K. Patel, H. Campbell, A. Schiavi, R. Snavely, S. C. Wilks, and O. Willi, Phys. Rev. Lett. **86**, 1769 (2001).
18. M. Hegelich, S. Karsch, G. Pretzler, D. Habs, K. Witte, W. Guenther, M. Allen, A. Blazevic, J. Fuchs, J. C. Gauthier, M. Geissel, P. Audebert, T. Cowan, and M. Roth, Phys. Rev. Lett. **89**, 085002 (2002).
19. M. Borghesi, A. J. Mackinnon, D. H. Campbell, D. G. Hicks, S. Kar, P. K. Patel, D. Price, L. Romagnani, A. Schivai, and O. Willi, Phys. Rev. Lett. **92**, 055003 (2004).
20. J. Schreiber, M. Kaluza, F. Grüner, U. Schramm, B. M. Hegelich, J. Cobble, M. Geissler, E. Brambrink, J. Fuchs, P. Audebert, D. Habs, and K. Witte, Appl. Phys. B **79**, 1041 (2004).
21. Y. Glinec, J. Faure, L. Le Dain, S. Darbon, T. Hosokai, J. J. Santos, E. Lefebvre, J.-P. Rousseau, F. Burgy, B. Mercier, and V. Malka, Phys. Rev. Lett. **94**, 025003 (2005).
22. M. M. Murnane, H. C. Kapteyn, M. D. Rosen, and R. W. Falcone, Science **251**, 531 (1991).

https://doi.org/10.1017/hpl.2019.35 Published online by Cambridge University Press

23. G. A. Mourou, C. P. Barty, and M. D. Perry, "Ultrahigh-intensity laser: physics of the extreme on a tabletop", Technical Report, Lawrence Livermore National Laboratory (1997).
24. S. M. Hooker, Nat. Photon. **7**, 775 (2013).
25. S. Chatziathanasiou, S. Kahaly, E. Skantzakis, G. Sansone, R. Lopez-Martens, S. Haessler, K. Varju, G. Tsakiris, D. Charalambidis, and P. Tzallas, *Photonics* (Multidisciplinary Digital Publishing Institute, 2017), p. 26.
26. O. Jahn, V. E. Leshchenko, P. Tzallas, A. Kessel, M. Krüger, A. Münzer, S. A. Trushin, G. D. Tsakiris, S. Kahaly, D. Kormin, L. Veisz, V. Pervak, F. Krausz, Z. Major, and S. Karsch, Optica **6**, 280 (2019).
27. A. G. Mordovanakis, J. Easter, N. Naumova, K. Popov, P.-E. Masson-Laborde, B. Hou, I. Sokolov, G. Mourou, I. V. Glazyrin, W. Rozmus, V. Bychenkov, J. Nees, and K. Krushelnick, Phys. Rev. Lett. **103**, 235001 (2009).
28. M. Thévenet, A. Leblanc, S. Kahaly, H. Vincenti, A. Vernier, F. Quéré, and J. Faure, Nat. Phys. **12**, 355 (2016).
29. M. Thévenet, H. Vincenti, and J. Faure, Phys. Plasmas **23**, 063119 (2016).
30. H. Habara, K. Ohta, K. A. Tanaka, G. Ravindra Kumar, M. Krishnamurthy, S. Kahaly, S. Mondal, M. K. Bhuyan, R. Rajeev, and J. Zheng, Phys. Rev. Lett. **104**, 055001 (2010).
31. H. Habara, K. Ohta, K. A. Tanaka, G. Ravindra Kumar, M. Krishnamurthy, S. Kahaly, S. Mondal, M. K. Bhuyan, R. Rajeev, and J. Zheng, Phys. Plasmas **17**, 056306 (2010).
32. A. Lifschitz, F. Sylla, S. Kahaly, A. Flacco, M. Veltcheva, G. Sanchez-Arriaga, E. Lefebvre, and V. Malka, New J. Phys. **16**, 033031 (2014).
33. S. Kahaly, F. Sylla, A. Lifschitz, A. Flacco, M. Veltcheva, and V. Malka, Sci. Rep. **6**, 31647 (2016).
34. S. V. Bulanov and V. S. Khoroshkov, Plasma Phys. Rep. **28**, 453 (2002).
35. S. V. Bulanov, T. Z. Esirkepov, V. S. Khoroshkov, A. V. Kuznetsov, and F. Pegoraro, Phys. Lett. A **299**, 240 (2002).
36. L. Disdier, J. P. Garconnet, G. Malka, and J. L. Miquel, Phys. Rev. Lett. **82**, 1454 (1999).
37. P. A. Norreys, A. P. Fews, F. N. Beg, A. R. Bell, A. E. Dangor, P. Lee, M. B. Nelson, H. Schmidt, M. Tatarakis, and M. D. Cable, Plasma Phys. Control. Fusion **40**, 175 (1998).
38. T. E. Cowan, M. D. Perry, M. H. Key, T. R. Ditmire, S. P. Hatchett, E. A. Henry, J. D. Moody, M. J. Moran, D. M. Pennington, T. W. Phillips, T. C. Sangster, J. A. Sefcik, M. S. Singh, R. A. Snavely, M. A. Stoyer, S. C. Wilks, P. E. Young, Y. Takahashi, B. Dong, W. Fountain, T. Parnell, J. Johnson, A. W. Hunt, and T. Kuhl, Laser Part. Beams **17**, 773 (1999).
39. C. Danson, D. Hillier, N. Hopps, and D. Neely, High Power Laser Sci. Eng. **3**, e3 (2015).
40. C. L. Haefner, A. Bayramian, S. Betts, R. Bopp, S. Buck, J. Cupal, M. Drouin, A. Erlandson, J. Horáček, J. Horner, J. Jarboe, J. Kasi, D. Kim, E. Koh, L. Koubikova, W. Maranville, C. Marshall, D. Mason, J. Menapace, P. Miller, P. Mazurek, A. Naylon, J. Novak, D. Peceli, P. Rossi, J. Schaffers, E. Sistrunk, D. Smith, T. Spinka, J. Stanley, R. Steele, C. Stolz, T. Suratwala, S. Telford, J. Thoma, D. VanBlarcom, J. Weiss, and P. Wegner, Proc. SPIE **10241**, 1024102 (2017).
41. E. Sistrunk, T. Spinka, A. Bayramian, S. Betts, R. Bopp, S. Buck, K. Charron, J. Cupal, R. Deri, M. Drouin, A. Erlandson, E. S. Fulkerson, J. Horner, J. Joracek, J. Jarboe, J. Kasl, D. Kim, E. Koh, L. Koubikova, R. Lanning, W. Maranville, C. Marshall, D. Mason, J. Menapace, P. Miller, P. Mazurek, A. Maylon, J. Novak, D. Peceli, P. Rosso, K. Schaffers, D. Smith, J. Stanley, R. Steele, S. Telford, J. Thoma, D. VanBlarcom, J. Weiss, P. Wegner, B. Rus, and C. Haefner, in *CLEO: Science and Innovations* (Optical Society of America, 2017), paper STh1L2.
42. B. Rus, P. Bakule, D. Kramer, J. Naylon, J. Thoma, M. Fibrich, J. T. Green, J. C. Lagron, R. Antipenkov, J. Bartoníček, F. Batysta, R. Base, R. Boge, S. Buck, J. Cupla, M. A. Drouin, M. Durak, B. Himmel, T. Havlicek, P. Homer, A. Honsa, M. Horacek, P. Hribek, J. Hubacek, Z. Hubka, G. Kalinchenko, K. Kasi, L. Indra, P. Korous, M. Koselja, L. Koubikova, M. Laub, T. Mazanec, A. Meadows, J. Novak, D. Peceli, J. Polan, D. Snopek, V. Sobr, P. Trojek, B. Tykalewicz, P. Velpula, E. Verhagen, S. Vyhlidka, J. Weiss, C. Haefner, A. Bayramian, S. Betts, T. Spinka, J. Stanley, C. Stolz, T. Suratwala, S. Telford, T. Ditmire, E. Gaul, M. Donovan, C. Frederickson, G. Friedman, D. Hammond, D. Hidinger, G. Cheriaux, A. Jochmann, M. Kepler, C. Malato, M. Maritnez, T. Metzger, M. Schultze, P. Mason, K. Ertel, A. Lintern, C. Edwards, C. Hernandez-Gomez, and J. Collier, Proc. SPIE **10241**, 102410J (2017).
43. S. Mondal, M. Shirozhan, N. Ahmed, M. Bocoum, F. Boehle, A. Vernier, S. Haessler, R. Lopez-Martens, F. Sylla, C. Sire, F. Quéré, K. Nelissen, C. Varjú, and S. Kahaly, J. Opt. Soc. Am. B **35**, A93 (2018).
44. S. Weber, S. Bechet, S. Borneis, L. Brabec, M. Bučka, E. Chacon-Golcher, M. Ciappina, M. DeMarco, A. Fajstavr, K. Falk, E.-R. Garcia, J. Grosz, Y.-J. Gu, J.-C. Hernandez, M. Holec, P. Janečka, M. Jantač, M. Jirka, H. Kadlecova, D. Khikhlukha, O. Klimo, G. Korn, D. Kramer, D. Kumar, T. Lastovička, P. Lutoslawski, L. Morejon, V. Olšovocová, M. Rajdl, O. Renner, B. Rus, S. Singh, M. Šmid, M. Sokol, R. Versaci, R. Vrána, M. Vranic, J. Vyskočil, A. Wolf, and Q. Yu, Matter Radiat. Extremes **2**, 149 (2018).
45. S. Kühn, M. Dumergue, S. Kahaly, S. Mondal, M. Füle, T. Csizmadia, B. Farkas, B. Major, Z. Várallyay, E. Cormier, M. Kalashikov, F. Calegari, M. Devetta, F. Frassetto, E. Månsson, L. Poletto, S. Stagira, C. Vozzi, M. Nisoli, P. Rudawski, S. Maclot, F. Campi, H. Wikmark, C. L. Arnold, C. M. Heyl, P. Johnsson, A. L'Huillier, R. Lopez-Martens, S. Haessler, M. Bocoum, F. Boehle, A. Vernier, G. Iaquaniello, E. Skantzakis, N. Papadakis, C. Kalpouzos, P. Tzallas, F. Lépine, D. Charalambidis, K. Varjú, K. Osvay, and G. Sansone, J. Phys. B: At. Mol. Opt. Phys. **50**, 132002 (2017).
46. W. Leemans, "Laser technology for k-BELLA and beyond", Technical Report, Lawrence Berkeley National Laboratory (2017).
47. I. Prencipe, J. Fuchs, S. Pascarelli, D. W. Schumacher, R. B. Stephens, N. B. Alexander, R. Briggs, M. Büscher, M. O. Cernaianu, A. Choukourov, M. DeMarco, A. Erbe, J. Fassbender, G. Fiquet, P. Fitzsimmons, C. Gheorghui, J. Hund, L. G. Huang, M. Harmand, N. J. Hartley, A. Irman, T. Kluge, Z. Konopkova, S. Kraft, D. Kraus, V. Leca, D. Margarone, J. Metzkes, K. Nagai, W. Nazarov, P. Putoslawski, D. Papp, M. Passoni, A. Pelka, J. P. Perin, J. Schulz, M. Smid, C. Spindloe, S. Steinke, R. Torchio, C. Vass, T. Wiste, R. Zaffino, K. Zeil, T. Tschentscher, U. Schramm, and T. E. Cowan, High Power Laser Sci. Eng. **5**, e17 (2017).
48. H. C. Kapteyn, M. M. Murnane, A. Szoke, and R. W. Falcone, Opt. Lett. **16**, 490 (1991).
49. R. K. Kirkwood, D. P. Turnbull, T. Chapman, S. C. Wilks, M. D. Rosen, R. A. London, L. A. Pickworth,

https://doi.org/10.1017/hpl.2019.35 Published online by Cambridge University Press

W. H. Dunlop, J. D. Moody, D. J. Strozzi, P. A. Michel, L. Divol, O. L. Landen, B. J. MacGowan, B. M. Van Wonterghem, K. B. Fournier, and B. E. Blue, Nat. Phys. **14**, 80 (2018).
50. A. Thoss, M. Richardson, G. Korn, M. Faubel, H. Stiel, U. Vogt, and T. Elsaesser, J. Opt. Soc. Am. B **20**, 224 (2003).
51. A. Thoß, "X-ray emission and particle acceleration from a liquid jet target using a 1-kHz ultrafast laser system", PhD. Thesis (Freie Universität Berlin, 2003).
52. L. Rayleigh, Proc. Lond. Math. Soc. **1**, 4 (1878).
53. H. M. Ryan, W. E. Anderson, S. Pal, and R. J. Santoro, J. Propul. Power **11**, 135 (1995).
54. K. R. Wilson, B. S. Rude, T. Catalano, R. D. Schaller, J. G. Tobin, D. T. Co, and R. J. Saykally, J. Phys. Chem. B **105**, 3346 (2001).
55. J. Eggers and E. Villermaux, Rep. Prog. Phys. **71**, 036601 (2008).
56. A. G. Darbyshire and T. Mullin, J. Fluid Mech. **289**, 83 (1995).
57. O. Reynolds, Philos. Trans. R. Soc. Lond. **174**, 935 (1883).
58. H. Faisst and B. Eckhardt, J. Fluid Mech. **504**, 343 (2004).
59. W. van Hoeve, S. Gekle, J. H. Snoeijer, M. Versluis, M. P. Brenner, and D. Lohse, Phys. Fluids **22**, 122003 (2010).
60. A. Kalaaji, B. Lopez, P. Attane, and A. Soucemarianadin, Phys. Fluids **15**, 2469 (2003).
61. W. T. Pimbley and H. C. Lee, IBM J. Res. Dev. **21**, 21 (1977).
62. P. Monot, T. Auguste, L. A. Lompré, G. Mainfray, and C. Manus, J. Opt. Soc. Am. B **9**, 1579 (1992).
63. A. Sullivan, H. Hamster, S. P. Gordon, R. W. Falcone, and H. Nathel, Opt. Lett. **19**, 1544 (1994).
64. T. Nayuki, Y. Oishi, T. Fujii, K. Nemoto, T. Kayoiji, Y. Okano, Y. Hironaka, K. G. Nakamura, K.-i. Kondo, and K. Ueda, Rev. Sci. Instrum. **74**, 3293 (2003).
65. M. Noaman-ul Haq, H. Ahmed, T. Sokollik, L. Yu, Z. Liu, X. Yuan, F. Yuan, M. Mirzaie, X. Ge, L. Chen, and J. Zhang, Phys. Rev. Accel. Beams **20**, 041301 (2017).
66. A. G. Mordovanakis, P.-E. Masson-Laborde, J. Easter, K. Popov, B. Hou, G. Mourou, W. Rozmus, M. G. Haines, J. Nees, and K. Krushelnick, Appl. Phys. Lett. **96**, 071109 (2010).
67. A. Borot, A. Malvache, X. Chen, A. Jullien, J.-P. Geindre, P. Audebert, G. Mourou, F. Quéré, and R. Lopez-Martens, Nat. Phys. **8**, 416 (2012).
68. J. T. Morrison, E. A. Chowdhury, K. D. Frische, S. Feister, V. Ovchinnikov, J. Nees, C. Orban, R. R. Freeman, and W. M. Roquemore, Phys. Plasmas **22**, 043101 (2015).
69. L. C. Mountford, R. A. Smith, and M. H. R. Hutchinson, Rev. Sci. Instrum. **69**, 3780 (1998).
70. J. B. Kim, S. Göde, and S. H. Glenzer, Rev. Sci. Instrum. **87**, 11E328 (2016).
71. M. Gauthier, C. B. Curry, S. Göde, F.-E. Brack, J. B. Kim, M. J. MacDonald, J. Metzkes, L. Obst, M. Rehwald, C. Rödel, H. P. Schlenvoigt, W. Schumaker, U. Schramm, K. Zeil, and S. H. Glenzer, Appl. Phys. Lett. **111**, 114102 (2017).
72. P. L. Poole, C. D. Andereck, D. W. Schumacher, R. L. Daskalova, S. Feister, K. M. George, C. Willis, K. U. Akli, and E. A. Chowdhury, Phys. Plasmas **21**, 063109 (2014).
73. P. L. Poole, C. Willis, G. E. Cochran, R. T. Hanna, C. D. Andereck, and D. W. Schumacher, Appl. Phys. Lett. **109**, 151109 (2016).
74. S. Feister, J. A. Nees, J. T. Morrison, K. D. Frische, C. Orban, E. A. Chowdhury, and W. M. Roquemore, Rev. Sci. Instrum. **85**, 11D602 (2014).
75. M. Ekimova, W. Quevedo, M. Faubel, P. Wernet, and E. T. J. Nibbering, Struct. Dyn. **2**, 054301 (2015).
76. G. Galinis, J. Strucka, J. C. T. Barnard, A. Braun, R. A. Smith, and J. P. Marangos, Rev. Sci. Instrum. **88**, 083117 (2017).
77. C. Orban, J. T. Morrison, E. A. Chowdhury, J. A. Nees, K. Frische, S. Feister, and W. M. Roquemore, Phys. Plasmas **22**, 023110 (2015).
78. G. K. Ngirmang, C. Orban, S. Feister, J. T. Morrison, K. D. Frische, E. A. Chowdhury, and W. M. Roquemore, Phys. Plasmas **23**, 043111 (2016).
79. S. Feister, D. R. Austin, J. T. Morrison, K. D. Frische, C. Orban, G. Ngirmang, A. Handler, J. R. H. Smith, M. Schillaci, J. LaVerne, E. A. Chowdhury, R. R. Freeman, and W. M. Roquemore, Opt. Express **25**, 18736 (2017).
80. C. A. Stan, D. Milathianaki, H. Laksmono, R. G. Sierra, T. A. McQueen, M. Messerschmidt, G. J. Williams, J. E. Koglin, T. J. Lane, M. J. Hayes, S. A. H. Guillet, M. Liang, A. L. Aquila, P. R. Willmott, J. Robinson, K. L. Gumerlock, S. Botha, K. Nass, I. Schlichting, R. L. Shoeman, H. A. Stone, and S. Boutet, Nat. Phys. **12**, 966 (2016).
81. A. R. Bell, J. R. Davies, S. Guerin, and H. Ruhl, Plasma Phys. Control. Fusion **39**, 653 (1997).
82. M. Schnürer, D. Hilscher, U. Jahnke, S. Ter-Avetisyan, S. Busch, M. Kalachnikov, H. Stiel, P. V. Nickles, and W. Sandner, Phys. Rev. E **70**, 056401 (2004).
83. S. Karsch, S. Düsterer, H. Schwoerer, F. Ewald, D. Habs, M. Hegelich, G. Pretzler, A. Pukhov, K. Witte, and R. Sauerbrey, Phys. Rev. Lett. **91**, 015001 (2003).
84. G. D. Martin, S. D. Hoath, and I. M. Hutchings, J. Phys.: Conf. Ser. **105**, 012001 (2008).
85. D. J. Perduijn, "Method of manufacturing jet nozzle ducts, and ink jet printer comprising a jet nozzle duct manufactured by means of the method", US Patent 4,418,354 (1983).
86. P. Chvykov, W. Ongg, J. Easter, B. Hou, J. Nees, and K. Krushelnick, J. Appl. Phys. **108**, 113301 (2010).
87. J. Yu, Z. Jiang, J. C. Kieffer, and A. Krol, Phys. Plasmas **6**, 1318 (1999).
88. B. Dromey, M. Zepf, A. Gopal, K. Lancaster, M. S. Wei, K. Krushelnick, M. Tatarakis, N. Vakakis, S. Moustaizis, R. Kodama, M. Tampo, C. Stoeckl, R. Clarke, H. Habara, D. Neely, S. Karsch, and P. Norreys, Nat. Phys. **2**, 456 (2006).
89. D. Hasson and R. E. Peck, AIChE J. **10**, 752 (1964).
90. Y. J. Choo and B. S. Kang, Exp. Fluids **31**, 56 (2001).
91. J. W. M. Bush and A. E. Hasha, J. Fluid Mech. **511**, 285 (2004).
92. J. D. Koralek, J. B. Kim, P. Bruza, C. B. Curry, Z. Chen, H. A. Bechtel, A. A. Cordones, P. Sperling, S. Toleikis, J. F. Kern, S. P. Moeller, S. H. Glenzer, and D. P. DePonte, Nat. Commun. **9**, 1353 (2018).
93. J. T. Morrison, S. Feister, K. D. Frische, D. R. Austin, G. K. Ngirmang, N. R. Murphy, C. Orban, E. A. Chowhury, and W. M. Roquemore, New J. Phys. **20**, 022001 (2018).
94. B. Hou, J. Nees, J. Easter, J. Davis, G. Petrov, A. Thomas, and K. Krushelnick, Appl. Phys. Lett. **95**, 101503 (2009).
95. C. Palmer, New J. Phys. **20**, 061001 (2018).
96. P. M. Nilson, W. Theobald, J. F. Myatt, C. Stoeckl, M. Storm, J. D. Zuegel, R. Betti, D. D. Meyerhofer, and T. C. Sangster, Phys. Rev. E **79**, 016406 (2009).
97. A. J. Mackinnon, Y. Sentoku, P. K. Patel, D. W. Price, S. Hatchett, M. H. Key, C. Andersen, R. Snavely, and R. R. Freeman, Phys. Rev. Lett. **88**, 215006 (2002).

https://doi.org/10.1017/hpl.2019.35 Published online by Cambridge University Press

98. D. T. Offermann, K. A. Flippo, S. A. Gaillard, D. C. Gautier, S. Letzring, J. C. Cobble, G. Wurden, R. P. Johnson, T. Shimada, D. S. Montgomery, R. P. Gonzales, T. Hurry, F. Archuleta, M. J. Schmitt, S. M. Reid, T. Bartal, M. S. Wei, D. P. Higginson, F. N. Beg, M. Geissel, and M. Schollmeier, J. Phys.: Conf. Ser. **244**, 022053 (2010).
99. H. Vincenti, S. Monchocé, S. Kahaly, G. Bonnaud, P. Martin, and F. Quéré, Nat. Commun. **5**, 3403 (2014).
100. A. Leblanc, S. Monchocé, C. Bourassin-Bouchet, S. Kahaly, and F. Quéré, Nat. Phys. **12**, 301 (2016).
101. A. Leblanc, S. Monchocé, H. Vincenti, S. Kahaly, J.-L. Vay, and F. Quéré, Phys. Rev. Lett. **119**, 155001 (2017).
102. K.-L. Pan, P.-C. Chou, and Y.-J. Tseng, Phys. Rev. E **80**, 036301 (2009).
103. G. L. Switzer, Rev. Sci. Instrum. **62**, 2765 (1991).
104. J. T. Morrison, M. Storm, E. Chowdhury, K. U. Akli, S. Feldman, C. Willis, R. L. Daskalova, T. Growden, P. Berger, T. Ditmire, L. Van Woerkom, and R. R. Freeman, Phys. Plasmas **19**, 030707 (2012).
105. S. Kar, H. Ahmed, R. Prasad, M. Cerchez, S. Brauckmann, B. Aurand, G. Cantono, P. Hadjisolomou, C. L. S. Lewis, A. Macchi, G. Nersisyna, A. P. L. Robinson, A. M. Schroer, M. Swantusch, M. Zepf, O. Willi, and M. Borghesi, Nat. Commun. **7**, 10792 (2016).
106. S. Backus, H. C. Kapteyn, M. M. Murnane, D. M. Gold, H. Nathel, and W. White, Opt. Lett. **18**, 134 (1993).
107. D. Panasenko, A. J. Shu, A. Gonsalves, K. Nakamura, N. H. Matlis, C. Toth, and W. P. Leemans, J. Appl. Phys. **108**, 044913 (2010).
108. D. W. Schumacher, P. L. Poole, C. Willis, G. E. Cochran, R. Daskalova, J. Purcell, and R. Heery, J. Instrum. **12**, C04023 (2017).
109. P. L. Poole, A. Krygier, G. E. Cochran, P. S. Foster, G. G. Scott, L. A. Wilson, J. Bailey, N. Bourgeois, C. Hernandez-Gomez, D. Neely, P. P. Rajeev, R. R. Freeman, and D. W. Schumacher, Sci. Rep. **6**, 32041 (2016).
110. E. Sani and A. DellfiOro, Opt. Mater. **37**, 36 (2014).
111. C. Ziener, P. S. Foster, E. J. Divall, C. J. Hooker, M. H. R. Hutchinson, A. J. Langley, and D. Neely, J. Appl. Phys. **93**, 768 (2003).
112. G. Doumy, F. Quéré, O. Gobert, M. Perdrix, P. Martin, P. Audebert, J. C. Gauthier, J.-P. Geindre, and T. Wittmann, Phys. Rev. E **69**, 026402 (2004).
113. C. Thaury, F. Quéré, J.-P. Geindre, A. Levy, T. Ceccotti, P. Monot, M. Bougeard, F. Réau, P. dfıOliveira, P. Audebert, R. Marjoribanks, and P. Martin, Nat. Phys. **3**, 424 (2007).
114. Y. Cai, W. Wang, C. Xia, J. Liu, L. Liu, C. Wang, Y. Xu, Y. Leng, R. Li, and Z. Xu, Phys. Plasmas **16**, 103104 (2009).
115. S. Inoue, K. Maeda, S. Tokita, K. Mori, K. Teramoto, M. Hashida, and S. Sakabe, Appl. Opt. **55**, 5647 (2016).
116. P. Heissler, E. Lugovoy, R. Hrlein, L. Waldecker, J. Wenz, M. Heigoldt, K. Khrennikov, S. Karsch, F. Krausz, B. Abel, and G. D. Tsakiris, New J. Phys. **16**, 113045 (2014).
117. E. Bliss, J. Hunt, P. Renard, G. Sommargren, and H. Weaver, IEEE J. Quantum Electron. **12**, 402 (1976).
118. M. Mlejnek, E. M. Wright, and J. V. Moloney, Phys. Rev. E **58**, 4903 (1998).
119. J. Sun and J. P. Longtin, J. Opt. Soc. Am. B **21**, 1081 (2004).
120. F. Paschen, Ann. Phys. **273**, 69 (1889).
121. S. Fujioka, H. Nishimura, K. Nishihara, M. Murakami, Y.-G. Kang, Q. Gu, K. Nagai, T. Norimatsu, N. Miyanaga, Y. Izawa, and K. Mima, Appl. Phys. Lett. **87**, 241503 (2005).
122. K. Takenoshita, C.-s. Koay, S. Teerawattanasook, and M. C. Richardson, *Emerging Lithographic Technologies VIII* (International Society for Optics and Photonics, 2004), p. 954.
123. A. K. Biń, Chem. Engng Sci. **48**, 3585 (1993).
124. X. Qu, A. Goharzadeh, L. Khezzar, and A. Molki, Exp. Therm. Fluid Sci. **44**, 51 (2013).
125. M. Knudsen, *The Kinetic Theory of Gases* (Metheun, London, 1934).
126. E. Hecht and A. Zajac, *Optics* (Addison-Wesley Publishing Company, 1974).
127. B. Dromey, D. Adams, R. Hörlein, Y. Nomura, S. G. Rykovanov, D. C. Carroll, P. S. Foster, S. Kar, K. Markey, P. McKenna, D. Neely, M. Geissler, G. D. Tsakiris, and M. Zepf, Nat. Phys. **5**, 146 (2009).
128. C. Rödel, D. an der Brügge, J. Bierbach, M. Yeung, T. Hahn, B. Dromey, S. Herzer, S. Fuchs, A. Galestian Pour, E. Eckner, M. Behmke, M. Cerchez, O. Jäckel, D. Hemmers, T. Toncian, M. C. Kaluza, A. Belyanin, G. Pretzler, O. Willi, A. Pukhov, M. Zepf, and G. G. Paulus, Phys. Rev. Lett. **109**, 125002 (2012).
129. S. Kahaly, S. Monchocé, H. Vincenti, T. Dzelzainis, B. Dromey, M. Zepf, P. Martin, and F. Quéré, Phys. Rev. Lett. **110**, 175001 (2013).
130. F. Quéré, C. Thaury, J. P. Geindre, G. Bonnaud, P. Monot, and P. Martin, Phys. Rev. Lett. **100**, 095004 (2008).
131. T. T. Luu, Z. Yin, A. Jain, T. Gaumnitz, Y. Pertot, J. Ma, and H. J. Wörner, Nat. Commun. **9**, 3723 (2018).
132. V. E. Fortov, Phys.-Usp. **50**, 333 (2007).
133. Y. Tsuboi, H. Fukumura, and H. Masuhara, Appl. Phys. Lett. **64**, 2745 (1994).
134. B. D. Strycker, M. M. Springer, A. J. Traverso, A. A. Kolomenskii, G. W. Kattawar, and A. V. Sokolov, Opt. Express **21**, 23772 (2013).
135. U. Weierstall, Philos. Trans. R. Soc. B: Biol. Sci. **369**, 20130337 (2014).
136. J. Kim, K. H. Kim, J. H. Lee, and H. Ihee, Acta Crystallogr. A **66**, 270 (2010).
137. F. Mafuné, K. Miyajima, K. Tono, Y. Takeda, J.-y. Kohno, N. Miyauchi, J. Kobayashi, Y. Joti, E. Nango, S. Iwata, and M. Yabashi, Acta Crystallogr. D **72**, 520 (2016).
138. J. W. Smith and R. J. Saykally, Chem. Rev. **117**, 13909 (2017).
139. M. Fondell, S. Eckert, R. M. Jay, C. Weniger, W. Quevedo, J. Niskanen, B. Kennedy, F. Sorgenfrei, D. Schick, E. Giangrisostomi, R. Ovsyannikov, K. Adamczyk, N. Huse, P. Wernet, R. Mitzner, and A. Fhlisch, Struct. Dyn. **4**, 054902 (2017).
140. C. Kleine, M. Ekimova, G. Goldsztejn, S. Raabe, C. Strufkber, J. Ludwig, S. Yarlagadda, S. Eisebitt, M. J. J. Vrakking, T. Elsaesser, E. T. J. Nibbering, and R. Arnaud, J. Phys. Chem. Lett. **10**, 52 (2018).
141. M. Ammann, L. Artiglia, and T. Bartels-Rausch, *Physical Chemistry of Gas–Liquid Interfaces* (Elsevier, 2018), p. 135.
142. F. Blanco, A. M. Roldán, K. Krupa, R. P. McEachran, R. D. White, S. Marjanović, Z. Lj Petrović, M. J. Brunger, J. R. Machacek, S. J. Buckman, J. P. Sullivan, L. Chiari, P. Limão-Vieira, and G. García, J. Phys. B: At. Mol. Opt. Phys. **49**, 145001 (2016).
143. W. Tattersall, L. Chiari, J. R. Machacek, E. Anderson, R. D. White, M. J. Brunger, S. J. Buckman, G. Garcia, F. Blanco, and J. P. Sullivan, J. Chem. Phys. **140**, 044320 (2014).

https://doi.org/10.1017/hpl.2019.35 Published online by Cambridge University Press